The Astrophysical Journal, 764:61 (30pp), 2013 February 10 doi:10.1088/0004-637X/764/1/61

A WATER MASER AND NH_3 SURVEY OF GLIMPSE EXTENDED GREEN OBJECTS

C. J. Cyganowski[1,11], J. Koda[2], E. Rosolowsky[3], S. Towers[2,4], J. Donovan Meyer[2], F. Egusa[5,6], R. Momose[7,8,9], and T. P. Robitaille[10]
[1] Harvard-Smithsonian Center for Astrophysics, Cambridge, MA 02138, USA; ccyganowski@cfa.harvard.edu
[2] Department of Physics and Astronomy, Stony Brook University, Stony Brook, NY 11794, USA
[3] Department of Physics and Astronomy, University of British Columbia, Okanagan, Kelowna BC V1V 1V7, Canada
[4] Department of Physics, Western Michigan University, Kalamazoo, MI 49008, USA
[5] Institute of Space and Astronautical Science, Japan Aerospace Exploration Agency, Chuo-ku, Sagamihara, Kanagawa 252-5210, Japan
[6] Department of Astronomy, California Institute of Technology, Pasadena, CA 91125, USA
[7] Department of Astronomy, University of Tokyo, Hongo, Bunkyo-ku, Tokyo 113-0033, Japan
[8] National Astronomical Observatory of Japan, Mitaka, Tokyo 181-8588, Japan
[9] Institute for Cosmic Ray Research, University of Tokyo, 5-1-5 Kashiwa-no-Ha, Kashiwa City, Chiba, 277-8582, Japan
[10] Max Planck Institute for Astronomy, Heidelberg, Germany
Received 2012 May 15; accepted 2012 October 12; published 2013 January 28

ABSTRACT

We present the results of a Nobeyama 45 m H_2O maser and NH_3 survey of all 94 northern GLIMPSE extended green objects (EGOs), a sample of massive young stellar objects (MYSOs) identified based on their extended 4.5 μm emission. We observed the NH_3(1,1), (2,2), and (3,3) inversion lines, and detected emission toward 97%, 63%, and 46% of our sample, respectively (median rms $\sim$ 50 mK). The H_2O maser detection rate is 68% (median rms $\sim$ 0.11 Jy). The derived H_2O maser and clump-scale gas properties are consistent with the identification of EGOs as young MYSOs. To explore the degree of variation among EGOs, we analyze subsamples defined based on mid-infrared (MIR) properties or maser associations. H_2O masers and warm dense gas, as indicated by emission in the higher-excitation NH_3 transitions, are most frequently detected toward EGOs also associated with both Class I and II CH_3OH masers. Ninety-five percent (81%) of such EGOs are detected in H_2O (NH_3(3,3)), compared to only 33% (7%) of EGOs without either CH_3OH maser type. As populations, EGOs associated with Class I and/or II CH_3OH masers have significantly higher NH_3 line widths, column densities, and kinetic temperatures than EGOs undetected in CH_3OH maser surveys. However, we find no evidence for statistically significant differences in H_2O maser properties (such as maser luminosity) among any EGO subsamples. Combining our data with the 1.1 mm continuum Bolocam Galactic Plane Survey, we find no correlation between isotropic H_2O maser luminosity and clump number density. H_2O maser luminosity is weakly correlated with clump (gas) temperature and clump mass.

Key words: infrared: ISM – ISM: jets and outflows – ISM: molecules – masers – stars: formation

Online-only material: color figures, extended figures, machine-readable tables

1. INTRODUCTION

The early stages of massive star formation remain poorly understood, due in part to the difficulty of identifying young massive young stellar objects (MYSOs)[12] that are actively accreting and driving outflows. Large-scale *Spitzer Space Telescope* surveys of the Galactic Plane have recently yielded a promising new sample of candidates: extended green objects (EGOs; Cyganowski et al. 2008), selected based on extended 4.5 μm emission, and named for the common coding of three-color Infrared Array Camera (IRAC; Fazio et al. 2004) images (RGB: 8.0, 4.5, 3.6 μm). Modeling, mid-infrared (MIR) spectroscopy, and narrowband near-infrared (NIR) imaging have shown that shock-excited molecular line emission, predominantly from H_2, can dominate the 4.5 μm broadband flux in active protostellar outflows (e.g., Smith & Rosen 2005; Smith et al. 2006; Davis et al. 2007; Ybarra & Lada 2009; Ybarra et al. 2010; De Buizer & Vacca 2010). While all the IRAC filters include H_2 lines, only the 4.5 μm band *lacks* polycyclic aromatic hydrocarbon (PAH) emission features (e.g., Figure 1 of Reach et al. 2006), which are readily excited in massive star-forming regions (MSFRs). Morphologically distinct extended 4.5 μm emission is thus a common feature of well-known MSFRs (e.g., DR21, S255N, NGC 6334I(N), G34.4+0.23, IRAS 18566+0408: Davis et al. 2007; Cyganowski et al. 2007; Hunter et al. 2006; Shepherd et al. 2007; Araya et al. 2007), and a means of identifying candidate MYSOs with active outflows.

Cyganowski et al. (2008, hereafter C08) cataloged over 300 EGOs in the Galactic Legacy Infrared Mid-Plane Survey Extraordinaire (GLIMPSE-I; Churchwell et al. 2009) survey area. At the time, the only data available for most EGOs were IR surveys. Using the GLIMPSE images, C08 divided cataloged EGOs into "likely" and "possible" outflow candidates based on the morphology and angular extent of their extended excess 4.5 μm emission. As detailed by C08, two phenomena in the IRAC images have the potential to be confused with moderately extended 4.5 μm emission: multiple nearby point sources and image artifacts near bright IRAC sources. To categorize the C08 EGOs, two observers independently reviewed three-color IRAC images: if either observer thought the MIR morphology could be attributable to one of these phenomena, the EGO was considered a "possible" outflow candidate. Of the 302 EGOs in the C08 catalog, 133 (44%) were classified as "likely" outflow candidates, 165 (55%) as "possible" outflow candidates, and 4 (1%) as "outflow-only" sources (in which the extended outflow emission could be readily separated from the central source). C08 also tabulated whether each EGO was or was

[11] NSF Astronomy and Astrophysics Postdoctoral Fellow.
[12] We define MYSOs as young stellar objects (YSOs) that will become O- or early B-type main-sequence stars ($M_{ZAMS} > 8\,M_\odot$).

not associated with an Infrared Dark Cloud (IRDC) visible against the diffuse 8 μm background. A majority (67%) of GLIMPSE EGOs are associated with IRDCs, which are thought to be sites of the earliest stages of massive star and cluster formation (e.g., Rathborne et al. 2006, 2007; Chambers et al. 2009; Wang et al. 2011). A somewhat higher fraction of EGO "likely" outflow candidates is found in IRDCs: 71% compared to 64% of "possible" outflow candidates (C08). The GLIMPSE survey is too shallow to detect distant low-mass outflows; based primarily on the MIR data, C08 argued that GLIMPSE EGOs were likely outflow-driving *massive* YSOs.

Testing this hypothesis required correlating extended 4.5 μm emission with other massive star formation tracers at high angular resolution. Interferometric studies at cm–mm wavelengths have provided much of the key evidence to date that EGOs are indeed young, massive YSOs driving active outflows. The first strong evidence was remarkably high detection rates for two diagnostic types of CH_3OH masers in sensitive, high angular resolution Very Large Array (VLA) surveys (Cyganowski et al. 2009, hereafter C09): 6.7 GHz Class II and 44 GHz Class I CH_3OH masers. Radiatively pumped by IR emission from warm dust, Class II CH_3OH masers are excited near the (proto)star (e.g., Cragg et al. 2005; Cyganowski et al. 2009 and references therein), and recent work suggests that the luminosities and relative strengths of different Class II transitions change as the central source evolves (e.g., Ellingsen et al. 2011; Breen et al. 2011 and references therein). The 6.7 GHz transition is the strongest and most common Class II CH_3OH maser; importantly, numerous searches have shown that these masers are *not* found toward low-mass YSOs (e.g., Minier et al. 2003; Bourke et al. 2005; Xu et al. 2008; Pandian et al. 2008). Collisionally excited in the presence of weak shocks, Class I CH_3OH masers are generally associated with molecular outflows and outflow/cloud interactions (e.g., Plambeck & Menten 1990; Kurtz et al. 2004; Voronkov et al. 2006), though recent work suggests Class I masers may also be excited by shocks driven by expanding H II regions (Voronkov et al. 2010). As a result of their association with outflows, Class I CH_3OH masers are more spatially distributed than Class II masers, and may be found many tens of arcseconds from the driving (proto)star (e.g., C09).

C09 detected 6.7 GHz CH_3OH masers toward $\gtrsim$64% of their 28 EGO targets, and 44 GHz CH_3OH masers toward ~90% of the subset searched for Class I emission (19 EGOs, 18 with 6.7 GHz CH_3OH masers). Their full sample of 28 EGOs was chosen to be visible from the northern hemisphere and to span a range in MIR properties including presence/absence of 8 and 24 μm counterparts, morphology, IRDC association, and angular extent of 4.5 μm emission. The 19 sources observed with the VLA at 44 GHz were all "likely" outflow candidates and, in essence, a 6.7 GHz CH_3OH maser-selected subsample (for further details, see C09). Subsequent high-resolution mm–λ observations of two of the C09 EGOs revealed high-velocity bipolar molecular outflows coincident with the 4.5 μm lobes, driven by compact millimeter continuum cores that exhibit hot core line emission (Cyganowski et al. 2011a, hereafter C11a). Recently, exceptionally deep VLA 3.6 and 1.3 cm continuum observations of a sample of 14 C09 EGOs have shown that the vast majority of the targets (12/14) are *not* ultracompact (UC) H II regions (Cyganowski et al. 2011b, hereafter C11b). Most (8/14) are undetected at both 3.6 and 1.3 cm ($\sigma \sim 30$ and 250 μJy beam^{-1}, respectively); four sources are associated with weak ($\lesssim$1 mJy) cm–λ emission consistent with hypercompact (HC) H II regions or ionized winds or jets. Based on their cm survey results and complementary multiwavelength data, C11b argued that these EGOs represent an early stage of massive star formation, before photoionizing feedback from the central MYSO becomes significant.

Detailed, high-resolution follow-up studies have, of necessity, been limited to relatively small EGO subsamples, and have generally focused on C08 "likely" outflow candidates (see also C09). Assessing the variation within the C08 catalog and the significance of their MIR classifications requires large, uniform surveys in tracers of dense gas and star formation activity. Few such surveys have been conducted to date. Chen et al. (2010) searched 88 (of 94) northern ($\delta \gtrsim -20^\circ$) EGOs for 3 mm HCO^+, ^{12}CO, ^{13}CO, and $C^{18}O$ emission, with the primary goal of detecting infall signatures. They found a larger "blue excess" toward EGOs associated with IRDCs compared to those not associated with IRDCs, and toward "possible" compared to "likely" outflow candidates; however, the interpretation of these results was complicated by the likelihood that multiple sources/dynamical phenomena were present within their large (~60–80″) beam. Recently, He et al. (2012) conducted a 1 mm line survey, covering ~251.5–252.5 GHz and ~260.2–261.2 GHz, toward 89 northern EGOs (resolution ~29″). He et al. (2012) focus on line width and line luminosity correlations, however, and do not analyze EGO subsamples. Chen et al. (2011, hereafter CE11) searched for 95 GHz Class I CH_3OH masers toward 192 northern and southern EGOs (of 302 total) with the MOPRA telescope ($\theta_{FWHP} \sim 36''$, $3\sigma \sim 1.6$ Jy). They found a higher 95 GHz CH_3OH maser detection rate toward "likely" than toward "possible" C08 EGOs (62% and 49%, respectively), and very similar detection rates toward EGOs associated/not associated with IRDCs (55%/53%). Their Class I CH_3OH maser detection rate is also much higher toward EGOs associated with Class II CH_3OH masers (80%) than toward those without (38%), consistent with the very high Class I maser detection rate of C09.

Like Class I CH_3OH masers, H_2O masers are collisionally pumped (e.g., Elitzur et al. 1989) and associated with protostellar outflows; notoriously variable, H_2O masers also often exhibit high-velocity emission features, offset by 30 km s^{-1} or more from the systemic velocity (e.g., Breen et al. 2010a; Caswell & Breen 2010). While Class I CH_3OH masers are excited under moderate conditions ($T \sim 80$ K, $n(H_2) \sim 10^5$–10^6 cm^{-3}, e.g., Leurini 2004) and associated with outflow-cloud interfaces, H_2O masers require more extreme conditions ($T \sim 400$ K, $n(H_2) \sim 10^8$–10^{10} cm^{-3}, Elitzur et al. 1989) and are thought to originate behind fast shocks in the inner regions of the outflow base. Numerous correlations have been reported between the properties of H_2O masers and those of the driving source or surrounding clump, including recent evidence that $L_{H_2O} \propto L_{bol}$ over many orders of magnitude (e.g., Urquhart et al. 2011; Bae et al. 2011). This suggests that H_2O masers may be used to investigate the properties of their driving sources, at least in a statistical sense for different subsamples—a possibility of interest for EGOs, since their bolometric luminosities are in most cases poorly constrained by available data (see also C11b).

Large H_2O maser and NH_3 surveys with single-dish telescopes have long been recognized as powerful tools for characterizing MSFRs (e.g., Churchwell et al. 1990; Anglada et al. 1996; Sridharan et al. 2002), and continue to be applied to new samples (e.g., Urquhart et al. 2011; Dunham et al. 2011b). NH_3 traces high-density gas (~10^4 cm^{-3}; e.g., Evans 1999; Stahler & Palla 2005), and provides a wealth of information about clump kinematics and physical properties; notably, it is an excellent

Table 1
EGO Sample: Properties from the Literature

Source Name	J2000 Coordinates[a]		EGO Catalog[a]	IRDC?[a]	CH_3OH Maser?[b]	
	α ($^{h\ m\ s}$)	δ ($^{\circ\ \prime\ \prime\prime}$)			Class II	Class I
G10.29−0.13	18 08 49.3	−20 05 57	2	Y	Y	Y
G10.34−0.14	18 09 00.0	−20 03 35	2	Y	Y	Y
G11.11−0.11	18 10 28.3	−19 22 31	3	Y	Y	N
G11.92−0.61	18 13 58.1	−18 54 17	1	Y	Y	Y
G12.02−0.21	18 12 40.4	−18 37 11	1	Y	N	N

Notes.
[a] From C08. The table number from C08 is given in the "EGO Catalog" column. Tables 1 and 2 of C08 listed "likely" outflow candidates. Tables 3 and 4 listed "possible" outflow candidates. Table 5 sources are those for which only "outflow-only" photometry was presented; we do not include them in our analysis of "likely" and "possible" subsamples.
[b] From CE11 (only). EGOs in our sample that are not included in CE11 are indicated by · · · . "–" indicates a source with a single-dish 6.7 GHz CH_3OH maser detection but no positional information, considered as having "no information" at 6.7 GHz by CE11 (see Section 3.1.1).

(This table is available in its entirety in a machine-readable form in the online journal. A portion is shown here for guidance regarding its form and content.)

"thermometer." This paper presents the results of a H_2O maser and NH_3 survey of the 94 northern ($\delta \gtrsim -20^\circ$) EGOs from the C08 catalog with the Nobeyama Radio Observatory 45 m telescope. The motivation for this survey was to characterize the properties of the C08 EGO sample as a whole, the main goals being to evaluate the significance of the MIR classifications from C08 and to place EGOs in the context of other large MYSO samples. We also compare the H_2O maser and NH_3 properties of EGO subsamples associated with Class I and/or II CH_3OH masers and explore correlations between H_2O maser and clump properties. Evolutionary interpretations have been suggested for both CH_3OH masers and H_2O maser properties (e.g., Ellingsen 2006; Ellingsen et al. 2007; Breen et al. 2010b; Breen & Ellingsen 2011), and our survey, in conjunction with the 1.1 mm Bolocam Galactic Plane Survey (BGPS; Aguirre et al. 2011; Rosolowsky et al. 2010), provides the necessary data to test these scenarios.

2. OBSERVATIONS AND DATA ANALYSIS

2.1. Nobeyama 45 m Observations

We targeted all 94 EGOs in the C08 catalog visible from Nobeyama (those in the northern Galactic plane, $\delta \gtrsim -20^\circ$). Our sample sources are listed in Table 1, along with information from the literature on their MIR properties and CH_3OH maser associations. The NH_3 $(J, K) = (1,1)$, (2,2), and (3,3) inversion transitions and the 22.235 GHz H_2O maser line were observed simultaneously with the Nobeyama Radio Observatory 45 m telescope (NRO45)[13] in 2008–2010. During our winter (January/February) observing sessions, the system temperature was typically ∼100–160 K. The beam size and main-beam efficiency of the NRO45 at 22 GHz are $\theta_{FWHP} = 73''$ and $\eta_{MB} = 0.825$, respectively. We pointed at the EGO positions tabulated in C08, which are the positions of the brightest 4.5 μm emission associated with each candidate outflow. We note that these positions will not necessarily be those of the driving sources (which in many cases are difficult to identify solely from the MIR data; see also C08), though in most cases the NRO beam is large enough to encompass likely driving sources as well as the 4.5 μm extent of the EGO.

We used the H22 receiver, a cooled HEMT receiver, and eight high-resolution acousto-optic spectrometers (AOSs) to observe both polarizations for each line simultaneously. The bandwidth and spectral resolution of the AOSs are 40 MHz and 37 kHz, respectively, corresponding to velocity coverage of ∼500 km s^{-1} and resolution of ∼0.5 km s^{-1} for the observed lines. The spectral channels were Nyquist-sampled.

The observations were conducted in position-switching mode, using "off" positions ∼5′ away. All spectra were checked for evidence of emission in the chosen "off" position, and, if necessary, reobserved. Initially, each target was observed for 2 minutes (on-source). The spectra were then inspected, and weak sources were reobserved to improve the signal-to-noise ratio as time permitted. The pointing was measured and adjusted at the beginning of each observing run using Galactic maser sources. The absolute pointing of the NRO45 is very accurate for 22 GHz observations, from a few arcsec (no wind) to ∼10″ in the windiest conditions in which we observed—still a small fraction of the beam size at 22 GHz.

The data reduction followed standard procedures using the NRO NEWSTAR software package (Ikeda et al. 2001). For each spectrum, emission-free channels were used to estimate and subtract a linear spectral baseline. For each line, the two polarizations were then co-added, weighted based on system temperature. The temperature scale was calibrated to the antenna temperature (T_A^*) in Kelvin with the standard chopper-wheel method, and the main-beam temperature (T_{MB}) calculated as $T_{MB} = T_A^*/\eta_{MB}$. For the H_2O maser data, we then convert to the Jansky scale to facilitate comparisons with other surveys.

Histograms of the rms are shown in Figure 1. The median 1σ rms is ∼50, 51, and 52 mK for NH_3(1,1), (2,2), and (3,3), respectively. For our H_2O maser observations, the median 1σ rms is ∼0.11 Jy, corresponding to a median 4σ detection limit of ∼0.44 Jy.

2.2. NH_3 Modeling and Physical Parameter Estimation

We estimate physical properties from the observed NH_3 spectra following the philosophy developed by Rosolowsky et al. (2008) and adapted for use in Dunham et al. (2010) and Dunham et al. (2011b). The emission is modeled as

[13] The 45 m radio telescope is operated by the Nobeyama Radio Observatory, a branch of the National Astronomical Observatory of Japan, National Institutes of Natural Sciences.

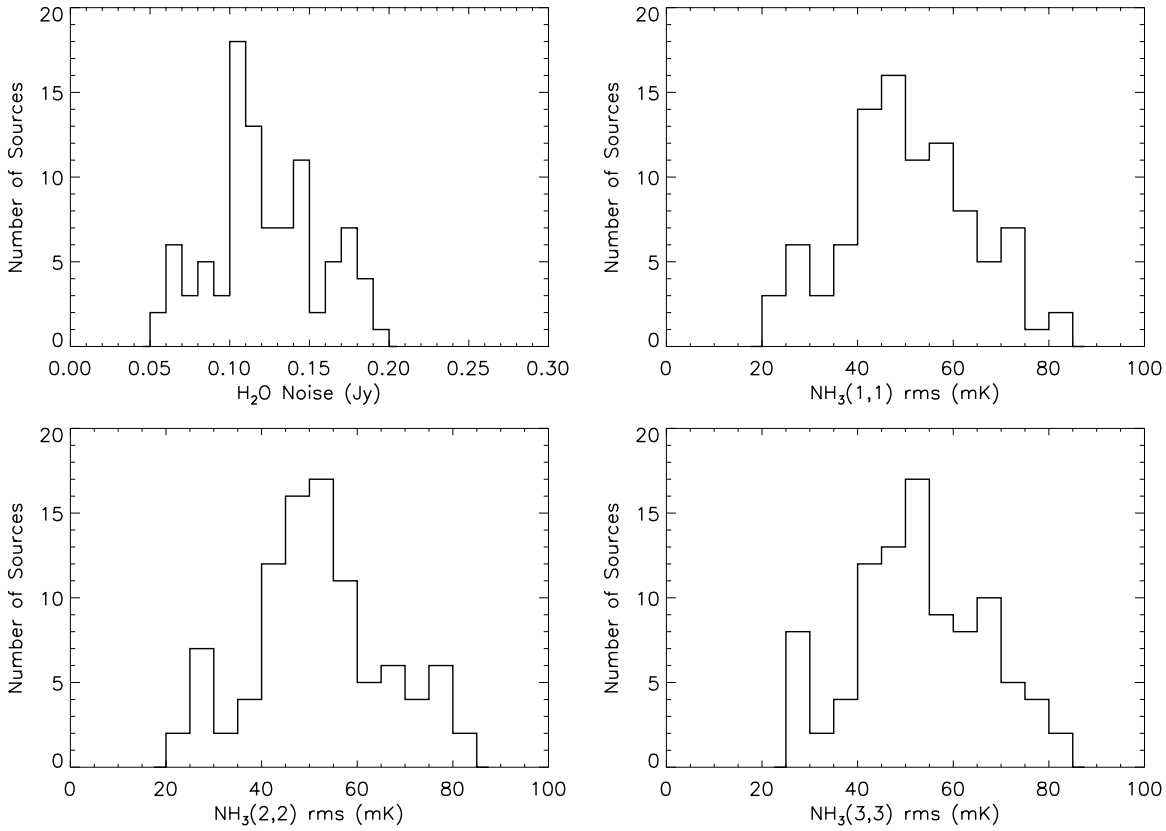

Figure 1. Histograms of the distributions of rms noise for the sources in our sample for the four observed lines.

a beam-filling slab of NH_3 with a variable column density (N_{NH3}), kinetic temperature (T_{kin}), excitation temperature (T_{ex}), Gaussian line width (σ_v), and LSR velocity (v_{LSR}). The model assumes the molecules are in thermodynamic equilibrium using an ortho-to-para ratio of 1:1, which is the high temperature formation limit (Takano et al. 2002). Hence, the ammonia molecules are partitioned among the energy levels as

$$Z_O = 1 + \sum_{J,K,i} 2(2J+1) \times \exp\left\{-\frac{h[BJ(J+1)+(C-B)J^2]+\Delta E(J,K,i)}{kT_k}\right\} \quad \text{for } J = K = 3, 6, 9, \ldots; i = 0, 1, \tag{1}$$

$$Z_P = \sum_{J,K,i} (2J+1) \times \exp\left\{-\frac{h[BJ(J+1)+(C-B)J^2]+\Delta E(J,K,i)}{kT_k}\right\} \quad \text{for } J = K = 1, 2, 4, 5, \ldots; i = 0, 1. \tag{2}$$

Here, J and K are the rotational quantum numbers of NH_3 and, for the metastable inversion transitions, $J = K$. The energy difference, $\Delta E(J, K, i)$, is the splitting of the symmetric and antisymmetric states, representing both levels of the inversion transition. The antisymmetric state, $\Delta E(J, K, 1)$, is $\Delta E/k \sim 1.1$ K above the symmetric state ($\Delta E(J, K, 0) = 0$). The column density of the molecules in the $N_{NH3}(J, K, i)$ ortho state is thus $N_{NH3} Z_O(J, i)/(2Z_O)$ and in the para state $N_{NH3} Z_P(J, i)/(2Z_P)$, where the factor of two arises because of the assumption of a 1:1 ortho-to-para ratio.

The optical depths in the individual transitions are calculated from the column densities in the individual states. The optical depth, hyperfine structure, velocity information and excitation conditions are then used to model the individual spectra. Free parameters are optimized using the MPFIT least-squares minimization routine including parameter bounds (Markwardt 2009). Uncertainties in the derived parameters are also determined from this optimization, accounting for the covariance between the parameters. We note that parameter uncertainties cannot account for systematic errors stemming from the uniform slab model being an incomplete description of the physical system. In all cases, derived quantities should be considered summary properties of the system and not a complete description. In most cases, this simple model reproduces the emission features observed on the large scales sampled.

For some sources in our sample, however, a single-slab model does not adequately represent the amplitudes of all three NH_3 transitions. Figure 2 shows examples of the two cases that prompted a revision of our model: (1) spectra that showed velocity components with different v_{LSR} or σ_v; and (2) spectra that could not be well represented by a single-temperature fit. We found that including a second component produced significantly better fits in these cases (see Rosolowsky et al. 2008, for more details). A second component was introduced for any fit where the χ^2 per degree of freedom was larger than two for any individual inversion line (23 sources, ~25% of our sample). For two sources that met this criterion, the best-fit two-component model included a component with an unphysically low excitation temperature (<2.73 K). For these sources (G14.33−0.64 and G19.36−0.03), we retain the single-component fits (leaving 21 sources with two-component fits). In the two-component model, the two slabs are nominally beam-filling, but no radiative transfer is performed from one slab through the other. We see no

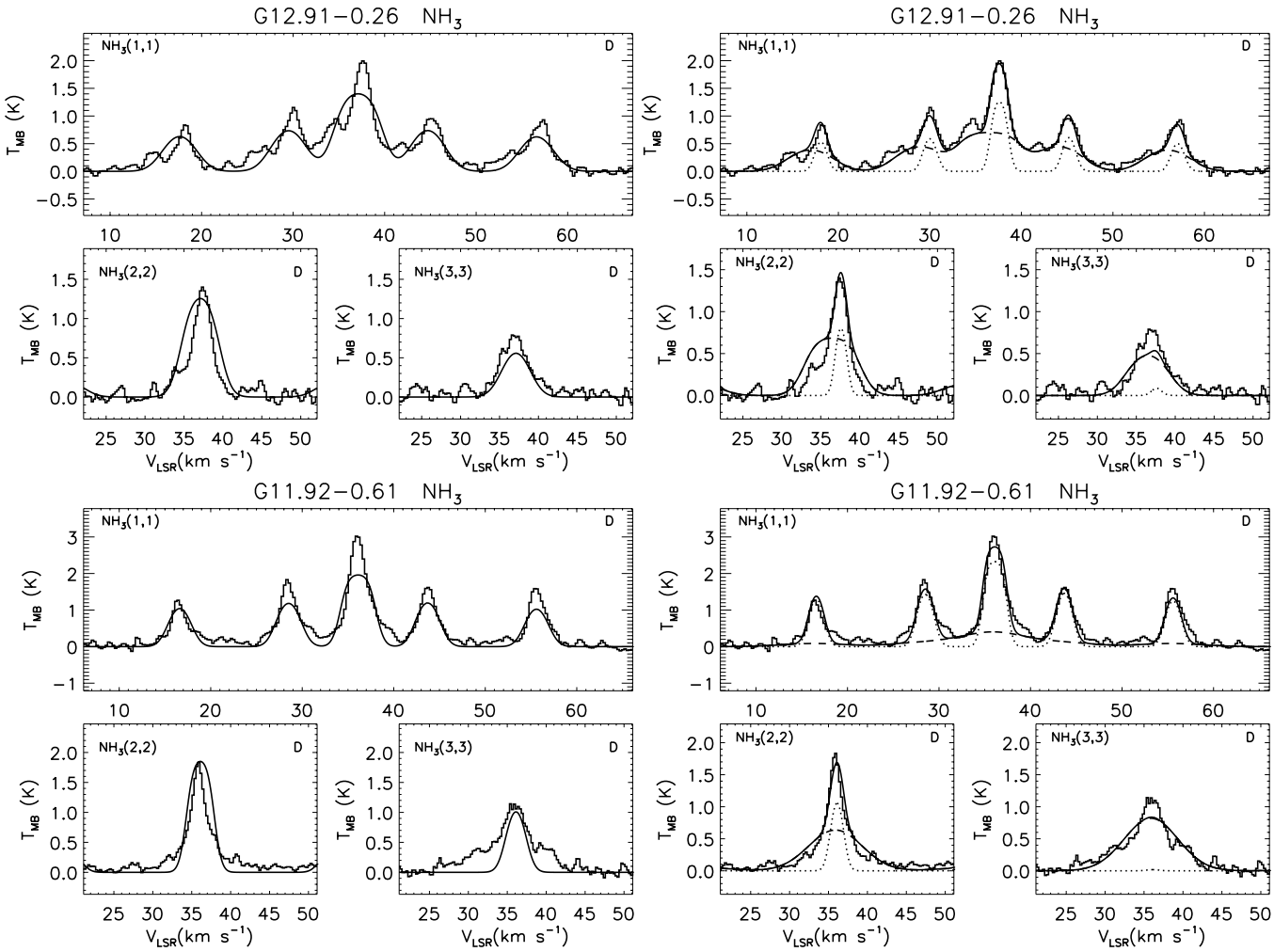

Figure 2. Single-component (left) and two-component (right) fits to sample NH_3 spectra. The best-fit models are overplotted on the observed spectra. For the two-component fits, model spectra for each component are shown (dashed line: warmer component; dotted line: cooler component), as well as their sum (solid line). The "D" at upper right in each panel indicates that our 4σ detection criterion was met for that transition. G12.91−0.26 (top) has two velocity components. For G11.92−0.61 (bottom), two temperature components significantly improve the fit to the NH_3(1,1), (2,2), and (3,3) spectra.

evidence for absorption of one component through the other in the spectra, suggesting such a treatment is not needed. A simple two-component fit yields a substantial improvement in the quality of the fit for many sources, successfully identifying two velocity/temperature components. We again note, however, that slab models are an incomplete description of the physical system; the best-fit physical parameters of the two components are thus likely representative but not definitive. We also note that a contradiction arises because the model takes $T_{\rm MB} = \eta_{\rm ff}(T_{\rm ex} - T_{\rm bg})(1 - e^{-\tau})$ where $\eta_{\rm ff} = 1$ is the assumed beam filling factor. However, the parameter $\eta_{\rm ff}$ is degenerate with $T_{\rm ex}$, and our assumption that $\eta_{\rm ff} = 1$ means $T_{\rm ex}$ is a lower limit. Relaxing this constraint on $\eta_{\rm ff}$ leaves $T_{\rm ex}$ undetermined for the two components, and suggests that the success of the simple two-component fitting means the two NH_3 components are spatially distinguished on smaller scales.

3. RESULTS

3.1. Detection Rates

3.1.1. Water Masers

We define a water maser detection as $>4\sigma$ emission in at least two adjacent channels. The overall detection rate is 68% (64/94), and Table 2 summarizes the H_2O maser detection rates toward various EGO subsamples. The uncertainties quoted in Table 2 were calculated using binomial statistics. Throughout, we treat each EGO separately, though we note that for EGOs separated on the sky by $\lesssim$36.″5 (half the FWHP Nobeyama beam), our data are insufficient to determine whether one or all are associated with H_2O masers. An unavoidable limitation of single-dish surveys is the possibility that some H_2O maser detections are chance alignments within the single-dish beam, and not physically associated with the target EGOs. While this can only be definitively addressed by future high-resolution observations of all detected EGOs, available data suggest that the effect on the sample as a whole is small. We searched the literature for reported H_2O masers with interferometric positions within 2′ of each EGO with a H_2O maser detection in our survey. Of 27 sources with such data available, there are only three cases ($\sim$11%) of H_2O masers within the Nobeyama beam and not associated with the EGO (see also Section 3.3).

One of the goals of this survey is to investigate whether the MIR EGO classifications from C08 correspond to differences in H_2O maser associations or dense gas properties. We find a somewhat higher H_2O maser detection rate for EGOs classified as "likely" MYSO outflow candidates, compared to those classified as "possible" outflow candidates based on their MIR

Table 2
Detection Statistics[a]

		NH_3 (1,1)		NH_3 (2,2)		NH_3 (3,3)[b]		Water Masers	
Category[c]	N_{obs}	N_{detect}	Rate	N_{detect}	Rate	N_{detect}	Rate	N_{detect}	Rate
Overall	94	91	0.97(0.02)	59	0.63(0.05)	43	0.46(0.05)	64	0.68(0.05)
IRDC Assoc.	47	47	1.00	35	0.74(0.06)	29	0.62(0.07)	29	0.62(0.07)
No IRDC Assoc.	47	44	0.94(0.04)	24	0.51(0.07)	14	0.30(0.07)	35	0.74(0.06)
"Likely"	48	47	0.98(0.02)	34	0.71(0.07)	29	0.60(0.07)	36	0.75(0.06)
"Possible"	43	41	0.95(0.03)	22	0.51(0.08)	12	0.28(0.07)	25	0.58(0.08)
"Outflow-only"	3	3	1.00	3	1.00	2	0.67(0.27)	3	1.00
Detected in:									
NH_3(1,1) only	32							14	0.44(0.09)
NH_3(1,1) and (2,2)	16							13	0.81(0.10)
NH_3(1,1), (2,2), and (3,3)	43							35	0.81(0.06)
Methanol Maser Associations[d]									
Class I	41	41	1.00	35	0.85(0.06)	31	0.76(0.07)	37	0.90(0.05)
Class I ND	28	25	0.89(0.06)	10	0.36(0.09)	3	0.11(0.06)	13	0.46(0.09)
Class II	28	27	0.96(0.04)	23	0.82(0.07)	18	0.64(0.09)	24	0.86(0.07)
Class II ND	23	22	0.96(0.04)	9	0.39(0.10)	6	0.26(0.09)	10	0.43(0.10)
Class I Only	8	8	1.00	6	0.75(0.15)	5	0.63(0.17)	5	0.63(0.17)
Class II Only	7	6	0.86(0.13)	4	0.57(0.19)	1	0.14(0.13)	4	0.57(0.19)
Class I and II	21	21	1.00	19	0.90(0.06)	17	0.81(0.09)	20	0.95(0.05)
Neither	15	14	0.93(0.06)	3	0.20(0.10)	1	0.07(0.06)	5	0.33(0.12)

Notes.
[a] Uncertainties in detection rates calculated using binomial statistics.
[b] Includes only sources detected in NH_3(1,1) and (2,2) as well as (3,3); see Section 3.1.2.
[c] IRDC associations and "likely/possible" designations from C08; see also Section 1.
[d] For consistency, all data on Class I and II CH_3OH maser associations are taken from Table 1 of CE11, see Section 3.1.1. "Class I": all EGOs with a Class I maser detection in CE11, regardless of Class II association (or lack of Class II information). "Class I ND": all EGOs listed as Class I nondetections in CE11, regardless of Class II association (or lack of Class II information). "Class II": all EGOs listed as Class II maser detections in CE11, regardless of Class I association. "Class II ND": all EGOs listed as Class II nondetections in CE11, regardless of Class I association. "Class I Only": EGOs listed as Class I detections and Class II nondetections in CE11. "Class II only": EGOs listed as Class I nondetections and Class II detections in CE11. "Class I and II": EGOs listed as both Class I and Class II detections in CE11. "Neither": EGOs listed as both Class I nondetections and Class II nondetections in CE11.

properties. Two-tailed binomial tests reject the null hypothesis that these two detection rates are the same at the 5% significance level (p-values $\sim$0.02). We also find a slightly higher H_2O maser detection rate toward EGOs *not* associated with IRDCs, compared to EGOs that are associated with IRDCs. In this case, however, two-tailed binomial tests are consistent with the detection rates being the same, at the 5% significance level (p-value = 0.07(0.10) adopting the non-IRDC(IRDC) detection rate as the null hypothesis). If, instead, EGOs are grouped based on the NH_3 transitions detected in our survey, much larger differences in the H_2O maser detection rates emerge. We detect H_2O masers toward only 44% of EGOs with NH_3(1,1) emission only, compared to 81% of EGOs with emission in the higher-excitation NH_3 transitions: a difference of nearly a factor of two.

There are comparably striking differences in the H_2O maser detection rates toward EGO subsamples defined based on CH_3OH maser associations (see Table 2). To group EGOs by their CH_3OH maser associations, we use the data in Table 1 of CE11. This dataset, derived from single-dish surveys, is the most uniform available that includes the majority ($\sim$3/4) of our northern EGO targets. CE11 searched for 95 GHz Class I CH_3OH masers toward 192 EGOs (northern and southern) with the MOPRA telescope ($\theta_{FWHP} \sim 36''$, $3\sigma \sim 1.6$ Jy). They also observed EGOs without known Class II masers at 6.7 GHz with the University of Tasmania Mt. Pleasant telescope ($\theta_{FWHP} \sim 7'$, $3\sigma \sim 1.5$ Jy). This produced a three-tiered classification for Class II maser associations: (1) EGOs associated with Class II masers, based on published high-resolution data (maser positions known to $\sim 1''$ or better); (2) EGOs for which 6.7 GHz emission was detected in the large Mt. Pleasant beam but no positional information was available ("no information"); and (3) EGOs undetected in the Mt. Pleasant observations. For this reason, definitive Class II maser information is available in CE11 for a smaller number of the EGOs in our sample (51) than for Class I masers (69 EGOs). We note one additional caveat. The 95 GHz Class I transition observed by CE11 is generally weaker than that at 44 GHz, and their MOPRA observations are significantly less sensitive than the VLA survey of C09. As a result, one source in the C09 sample that has weak 44 GHz Class I masers (G37.48−0.10) is listed as a Class I nondetection in CE11.

The most dramatic difference in H_2O maser detection rates in our survey is between EGOs associated with both Class I and II CH_3OH masers (20/21 $\sim$ 95%) and EGOs associated with neither type of CH_3OH maser (5/15 $\sim$ 33%). The H_2O maser detection rate is also very high ($\sim$90%) toward EGOs with Class I CH_3OH masers (considering all Class I detections, regardless of Class II detections/information). This correlation is consistent with both Class I CH_3OH and H_2O masers being associated with outflows, though H_2O masers are also observed toward $\sim$46% of EGOs undetected at 95 GHz. Unfortunately, comparison of "Class I only" and "Class II only" EGO subsamples is limited by the small number statistics.

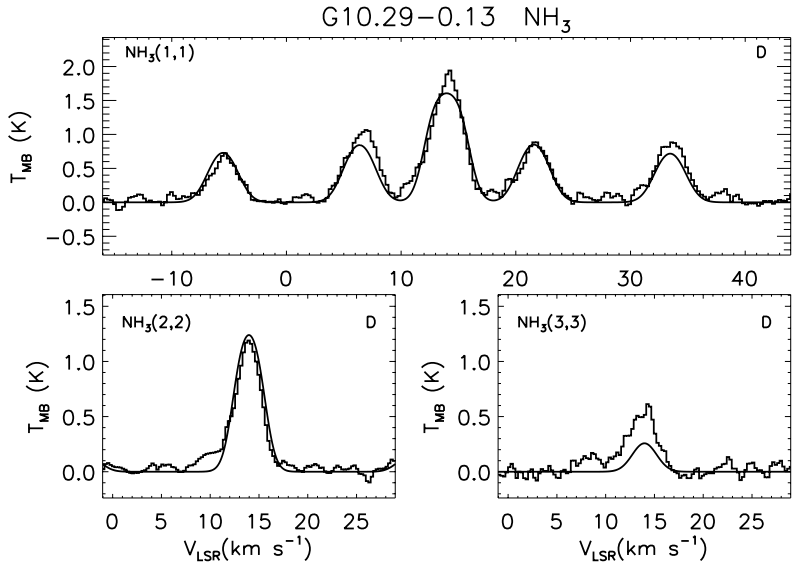

Figure 3. Observed NH_3 spectra with best-fit single-component model overlaid. A "D" in the upper right corner of a panel indicates that our 4σ detection criterion was met for that transition.

(An extended version of this figure is available in the online journal.)

3.1.2. NH_3

The vast majority (97%) of our target EGOs are detected in $NH_3(1,1)$ at the 4σ level (peak/rms). For a significant fraction (34%) of our sample, (1,1) is the only NH_3 transition detected.[14] As shown in Table 2, it is the detection rates for the higher-energy transitions, particularly (3,3), that show significant differences across EGO subsamples. The $NH_3(3,3)$ detection rate toward EGOs associated with IRDCs is about twice that for non-IRDC EGOs; similarly, the detection rate toward "likely" outflow candidates (as classified by C08) is about twice that for "possible" outflow candidates. The (2,2) detection rates show the same trends.

The strongest correlation we see, however, is again with CH_3OH maser associations. The highest (3,3) detection rate of any subsample is 81%, toward EGOs with both Class I and II CH_3OH masers, while the lowest (7%) is toward EGOs without either type. The (3, 3) detection rate toward EGOs with Class I masers (regardless of Class II association/information) is also high, at 76%. The (2,2) and (3,3) detection rates show similar trends, with (3,3) showing larger differences between subsamples.

3.1.3. NH_3 Nondetections

Our extremely high $NH_3(1,1)$ detection rate raises the question of whether the three nondetections are in some way unusual, or interlopers in the EGO sample. The (1,1) nondetections do have some common characteristics: they are not associated with IRDCs and do not have Class I CH_3OH masers. Two have detected H_2O maser emission in our survey. G49.42+0.33, a C08 "likely" outflow candidate, was included in the C09 sample and detected in thermal HCO^+(3–2), $H^{13}CO^+$(3–2), and CH_3OH ($5_{2,3}$–$4_{1,3}$) emission with the James Clerk Maxwell Telescope. Thus, there is dense gas associated with the EGO: in combination with the detection of Class II CH_3OH (C09) and H_2O masers (Table 6), strong evidence for the presence of MYSO(s). This EGO is among the most distant in our sample, so our Nobeyama NH_3 nondetection may be attributable to sensitivity and/or beam dilution.

We also detect H_2O maser emission toward G53.92-0.07, a C08 "possible" outflow candidate. Its MIR morphology is unusual amongst the EGO sample; the "green" source appears embedded in an 8 μm bright pillar, and the 4.5 μm emission is only slightly extended. Little is known about this source beyond its identification as an EGO and its association with a BGPS 1.1 mm source, but it is possible it may be a comparatively evolved outlier in the EGO sample.

Finally, G57.61+0.02 is a "possible" outflow candidate located on the edge of an 8 and 24 μm bright nebula, likely a more evolved source (e.g., compact or UC H II region). Formally undetected by our 4σ criterion, we do see a weak ($\sim 3.9\sigma$) $NH_3(1,1)$ line in our spectrum (see also Section 3.2.1).

3.2. NH_3 Properties

Table 3 presents the physical properties obtained from the single-component NH_3 modeling for all EGOs detected in NH_3 emission in our survey. The $NH_3(1,1)$, (2,2), and (3,3) peaks (T_{MB}) are also listed, with 4σ upper limits given for undetected transitions (for all sources, including NH_3 nondetections). If $NH_3(2,2)$ is not detected, the best-fit T_{kin} is treated as an upper limit and is indicated as such in Table 3. The observed NH_3 spectra for each detected source, overlaid with the best-fit model, are shown in Figure 3 (available online in its entirety), and the property distributions for our EGO sample are shown in Figure 4. Throughout, the $NH_3(1,1)$ peak (T_{MB}), σ_v, $\tau_{(1,1)}$, η_{ff}, and NH_3 column density are presented for all EGOs detected in $NH_3(1,1)$ emission. In Figure 4, the T_{kin} and $NH_3(2,2)$ peak distributions include only sources with $>4\sigma$ $NH_3(2,2)$ detections, and the $NH_3(3,3)$ peak distribution includes only sources with $>4\sigma$ detections in all three NH_3 transitions. For EGOs for which a two-component model provides a better fit to the observed NH_3 emission (Section 2.2), Figure 5 (available online in its entirety) shows the spectra overlaid with the best-fit two-component model, and Table 4 presents the parameters of the two-component fits.

[14] One source meets our 4σ peak/rms detection criterion for $NH_3(1,1)$ and (3,3), but not (2,2). This could be indicative of nonthermal (3,3) emission; however, the NH_3 emission is weak and the (3,3) detection is marginal ($<5\sigma$). Thus, we conservatively treat this source as an $NH_3(1,1)$-only detection in our analysis of detection rates and in Table 2.

Table 3
NH_3 Properties: Single-component Fits[a]

Source Name	v_{LSR} (km s^{-1})	σ_v (km s^{-1})	Distance[b] (kpc)	$T_{MB}(1,1)$[c] (K)	$\tau_{(1,1)}$	$N(NH_3)$ (cm^{-2}) $\times 10^{14}$	η_{ff}	T_{ex} (K)	T_{kin}[d] (K)	$T_{MB}(2,2)$[c] (K)	$T_{MB}(3,3)$[c] (K)	2 comp?[e]	H_2O Maser?
G10.29−0.13	13.97(0.01)	1.18(0.01)	1.58(+0.86, −1.13)	1.94(0.04)	4.76	22.1(0.6)	0.096(0.002)	4.52(0.05)	21.19(0.17)	1.19(0.04)	0.61(0.05)	Y	Y
G10.34−0.14	12.02(0.02)	1.07(0.02)	1.29(+0.92, −1.23)	1.56(0.06)	4.28	18.2(1.0)	0.047(0.002)	3.95(0.07)	28.23(0.38)	0.94(0.05)	0.76(0.07)	Y	Y
G11.11−0.11	29.79(0.02)	0.68(0.01)	12.67(+0.48, −0.41)[f]	1.79(0.07)	5.15	11.9(0.6)	0.150(0.006)	4.45(0.09)	14.15(0.27)	0.65(0.06)	0.32(0.07)	Y	N
G11.92−0.61	36.11(0.01)	1.09(0.01)	3.48(+0.44, −0.52)	3.02(0.07)	6.40	31.7(0.8)	0.087(0.001)	4.79(0.04)	26.27(0.19)	1.83(0.06)	1.14(0.07)	Y	Y
G12.02−0.21	−3.15(0.06)	1.04(0.05)	5.30(+0.20, −0.20)[g]	0.46(0.06)	5.18	13.2(2.1)	0.042(0.004)	3.16(0.15)	<12.85	<0.19	<0.22	N	N
G12.20−0.03	51.16(0.06)	1.24(0.05)	11.70(+0.31, −0.27)[f]	0.55(0.06)	3.76	13.5(2.3)	0.032(0.004)	3.27(0.13)	19.56(0.76)	0.28(0.05)	<0.25	N	Y

Notes.

[a] Uncertainties are given in parentheses. For kinematic distances, the uncertainties are based on the prescription of Reid et al. (2009; see also Section 3.2.1); for maser parallax distances, the uncertainties are taken from the cited reference. For the NH_3(1,1), (2,2), and (3,3) peak temperatures, the quoted uncertainty is the 1σ rms. For all other quantities, the uncertainties are estimated from the model optimization, and uncertainties of 0.00 indicate the case $T_{kin} = T_{ex}$ (see Section 2.2).

[b] Near kinematic distance estimated using the NH_3 v_{LSR}, except as otherwise noted. See also Section 3.2.1.

[c] Peak temperature of the NH_3 emission on the T_{MB} scale. All upper limits are 4σ.

[d] T_{kin} is indicated as an upper limit if NH_3(2,2) emission is not detected at $>4\sigma$.

[e] Indicates whether a two-component model was fit (Section 2.2). If "Y," the two-component model results are listed in Table 4.

[f] Associated with a 6.7 GHz CH_3OH maser assigned the far distance by Green & McClure-Griffiths (2011). Except for G12.20−0.03 and G45.80−0.36, all far distance assignments are "B" classifications in their scheme (see also Section 3.2.1). We adopt the far kinematic distance estimated from the NH_3 v_{LSR}.

[g] The longitude and velocity of this source indicate that it is likely in the near 3 kpc arm (see, for example, Figure 1 of Green et al. 2009). Following Green & McClure-Griffiths (2011), we place this source on a circle of radius 3.4 kpc around the Galactic Center, and adopt a distance uncertainty of ±0.2 kpc.

[h] Maser parallax distance. References: G14.33−0.64, Sato et al. (2010). G23.01−0.41, Brunthaler et al. (2009). G34.39+0.22 and G34.41+0.24, Kurayama et al. (2011). G35.20−0.74, Zhang et al. (2009).

[i] It is unclear if this source is at the near or the far distance (e.g., Cyganowski et al. 2011a; Green & McClure-Griffiths 2011).

[j] Source that meets 4σ detection criterion for NH_3(1,1) and (3,3), but not (2,2); hence, T_{kin} is treated as an upper limit as for other (2,2) nondetections. See also Section 3.1.2.

[k] NH_3 nondetection. G49.42+0.33: distance estimated using $H^{13}CO^+$ velocity from C09. G53.92−0.07: distance estimated using H_2O maser peak velocity. G57.61+0.02: distance estimated from velocity of weak (3.9σ) NH_3(1,1) emission below our 4σ detection threshold. The distance for G57.61+0.02 is included here and in Figure 4 for completeness, but this source is otherwise excluded from our analysis. See also Section 3.2.1.

[l] This temperature limit is likely excessively low because the criteria of least-squares fitting are failing and the error distributions are non-Gaussian.

(This table is available in its entirety in a machine-readable form in the online journal. A portion is shown here for guidance regarding its form and content.)

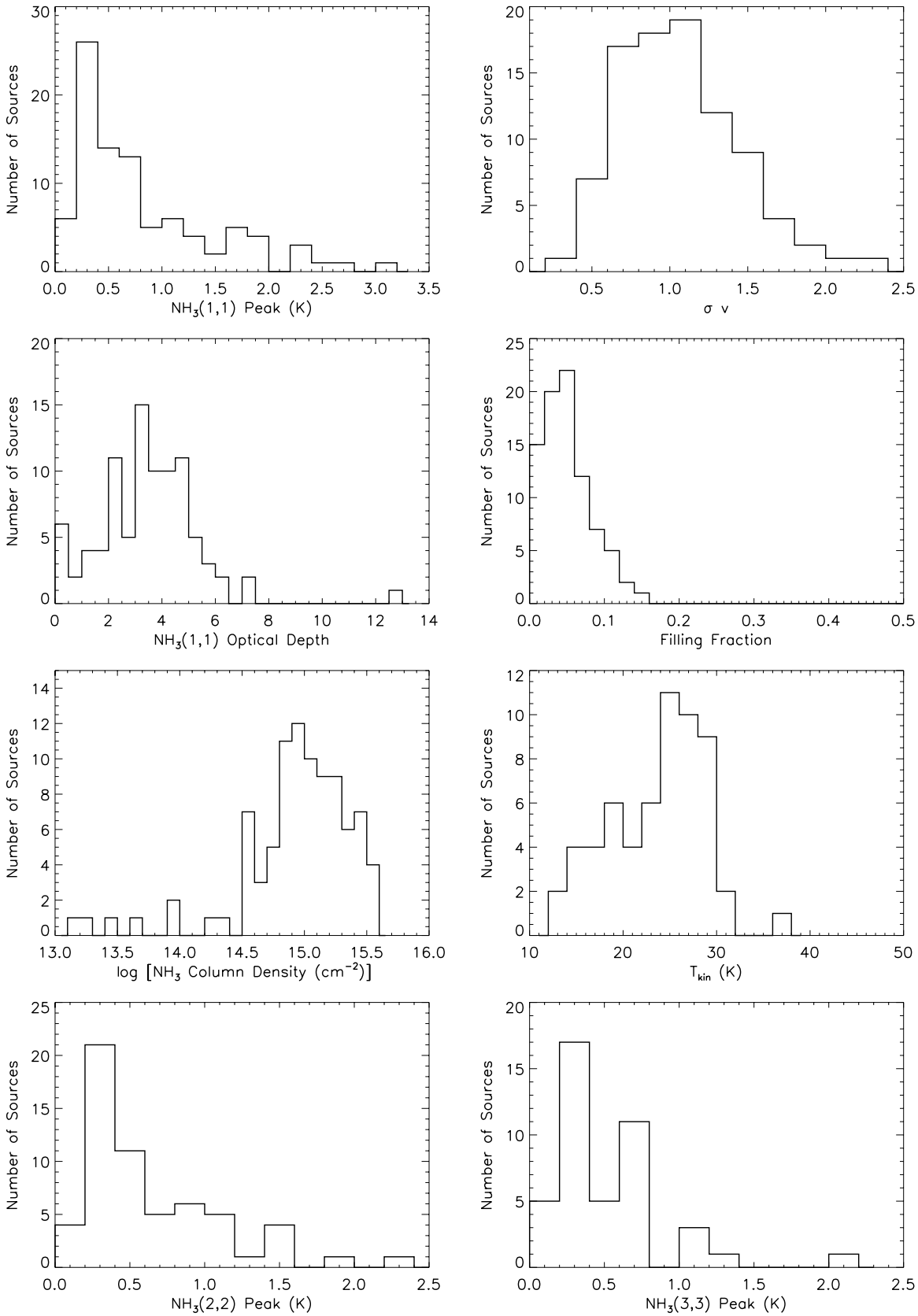

Figure 4. Histograms showing distributions of observed NH_3 properties and physical properties obtained from the NH_3 modeling. Bin sizes are 0.2 K for the NH_3 peak temperatures, 0.2 km s^{-1} for σ_v, 0.5 for $\tau_{(1,1)}$, 0.02 for η_{ff}, 0.1 dex for the NH_3 column density, and 2 K for T_{kin}. All EGOs detected in NH_3(1,1) are included in the first five panels ((1,1) peak, σ_v, $\tau_{(1,1)}$, η_{ff}, and column density). Sources for which $T_{ex} = T_{kin}$ (the upper limit, for $\eta_{ff} = 1$) are excluded from the filling fraction plot. EGOs detected in both NH_3(1,1) and (2,2) are included in the T_{kin} and (2,2) peak histograms, and EGOs detected in all three NH_3 transitions are included in the (3,3) peak plot.

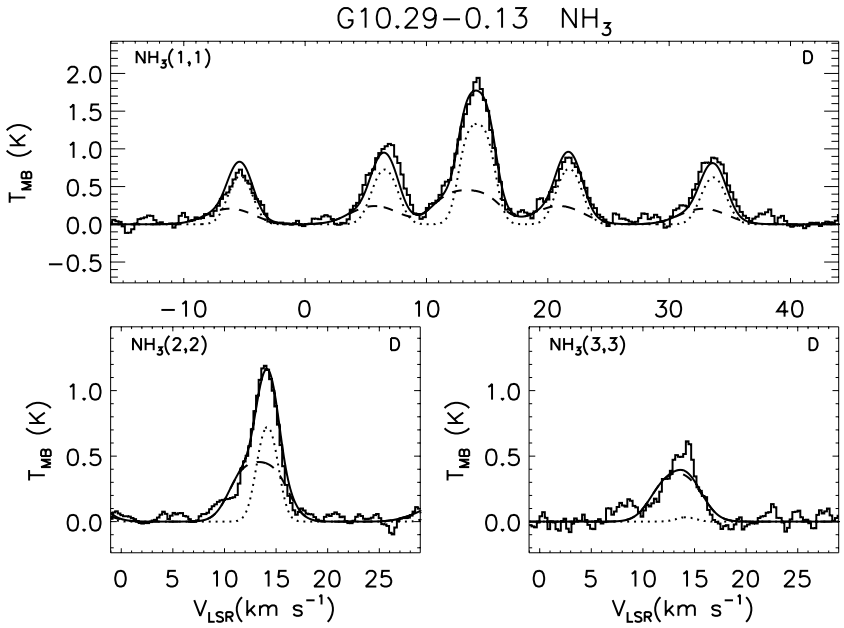

Figure 5. Observed NH_3 spectra with best-fit two-component model overlaid. Model spectra for each component are shown (dashed line: warmer component; dotted line: cooler component), as well as their sum (solid line). A "D" in the upper right corner of a panel indicates that our 4σ detection criterion was met for that transition.

(An extended version of this figure is available in the online journal.)

Table 4
NH_3 Properties: Two-component Fits[a]

Source Name	T_{kin} (K)	v_{LSR} (km s^{-1})	σ_v (km s^{-1})	T_{ex} (K)	$N(NH_3)$ (cm^{-2}) $\times 10^{14}$
G10.29−0.13	15.93(0.32)	14.16(0.02)	0.89(0.02)	4.19(0.06)	15.6(0.7)
	32.91(0.98)	13.31(0.06)	1.73(0.04)	3.23(0.12)	30.2(2.8)
G10.34−0.14	15.62(0.78)	12.05(0.03)	0.70(0.04)	4.04(0.17)	6.5(1.1)
	41.51(2.42)	12.05(0.05)	1.43(0.05)	3.32(0.23)	21.3(2.7)
G11.11−0.11	13.90(0.58)	29.40(0.04)	0.45(0.03)	3.70(0.25)	10.6(1.1)
	14.07(0.64)	30.33(0.14)	0.65(0.06)	3.72(0.22)	8.8(1.2)
G11.92−0.61	13.55(0.20)	36.10(0.01)	0.73(0.01)	5.16(0.07)	19.3(0.6)
	54.06(1.38)	35.89(0.06)	3.43(0.07)	54.06(0.00)	3.4(0.1)
G12.68−0.18	14.19(0.48)	56.42(0.04)	0.90(0.02)	3.55(0.11)	16.5(1.0)
	31.47(0.78)	54.99(0.04)	1.08(0.03)	3.33(0.10)	36.7(2.0)

Note. [a] Uncertainties estimated from the model optimization are given in parentheses: values of 0.00 indicate cases where the model is poorly constrained (see Section 2.2).

(This table is available in its entirety in a machine-readable form in the online journal. A portion is shown here for guidance regarding its form and content.)

3.2.1. Kinematic Distances

We calculate kinematic distances based on the NH_3 velocities in Table 3 and the prescription of Reid et al. (2009), using updated input parameters (M. Reid 2012, private communication; Galactic: $R_O = 8.40$ kpc, $\Theta_0 = 245.0\,\mathrm{km\,s^{-1}}$, $d\Theta/dr = 1.0\,\mathrm{km\,s^{-1}\,kpc^{-1}}$; Solar: $U_0 = 10.00\,\mathrm{km\,s^{-1}}$, $V_0 = 12.00\,\mathrm{km\,s^{-1}}$, $W_0 = 7.20\,\mathrm{km\,s^{-1}}$; Source peculiar motions: $U_S = 5.00\,\mathrm{km\,s^{-1}}$, $V_S = -6.00\,\mathrm{km\,s^{-1}}$, $W_S = 0.00\,\mathrm{km\,s^{-1}}$; and an assumed v_{LSR} uncertainty of $7\,\mathrm{km\,s^{-1}}$). For sources with distance ambiguities, the near kinematic distance is listed in Table 3, unless otherwise noted. The angular extent of EGOs on the sky supports adopting the near kinematic distance, as does the association of EGOs, as a population, with IRDCs (see also C08, C09). In their H I self-absorption study of 6.7 GHz CH_3OH masers, Green & McClure-Griffiths (2011) have recently suggested assigning the far distance to masers associated with a few (eight) of our targets. Most of these assignments are "Class B" in their scheme, reflecting uncertainty in the classification. For these sources, we adopt the far distance calculated from the NH_3 velocity. Maser parallax distances are adopted when available, as noted in Table 3.

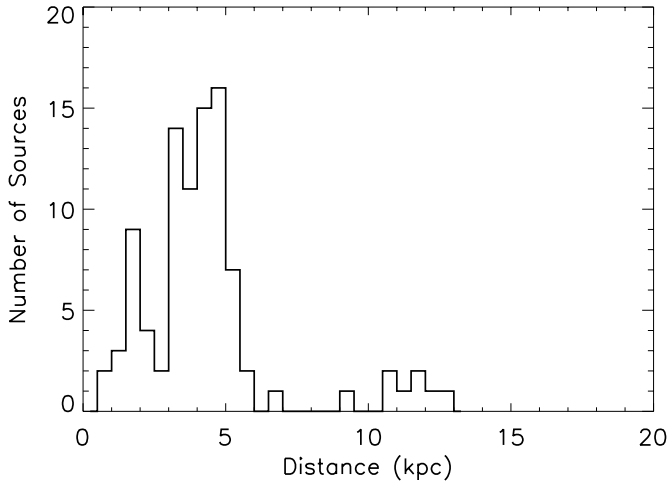

Figure 6. Distribution of adopted distances for all sources in our sample (3.2.1). The bin size is 0.5 kpc.

Three sources are undetected in $NH_3(1,1)$, and so present special cases for calculating kinematic distances. For G49.42+0.33, we use the $H^{13}CO^+(3–2)$ velocity from C09 (see also Section 3.1.3). For G53.92−0.07, the H_2O maser emission is very narrow ($\Delta v = 1.3\,\mathrm{km\,s^{-1}}$), and we calculate a kinematic distance using the H_2O maser peak velocity (Table 6). In G57.61+0.02, we detect weak $NH_3(1,1)$ emission at $\sim 3.9\sigma$, just below our formal detection limit. The fitted v_{LSR} of $37.4 \pm 0.1\,\mathrm{km\,s^{-1}}$ gives a kinematic distance of 4.50 ± 1.96 kpc. For completeness, we include this source in the distance histogram shown in Figure 6, but not in the subsequent analysis. The mean(median) distance for our sample is 4.3 kpc (4.2 kpc).

Table 5
EGO Subsamples with Statistically Significant Differences in NH_3 Properties

Subsample	Property	K-S Significance
Likely/Possible	$NH_3(1,1)$ peak (T_{MB})	8.4E-03
Likely/Possible	$NH_3(2,2)$ peak (T_{MB})	7.6E-03
IRDC/no IRDC	$NH_3(1,1)$ peak (T_{MB})	1.5E-05
IRDC/no IRDC	σ_v	8.2E-04
IRDC/no IRDC	η_{ff}	1.7E-03
H_2O maser detections/nondetections	σ_v	5.5E-08
H_2O maser detections/nondetections	$N(NH_3)$	1.6E-04
H_2O maser detections/nondetections	T_{kin}	4.7E-03
Class I/Class I ND	$NH_3(1,1)$ peak (T_{MB})	3.0E-03
Class I/Class I ND	σ_v	5.1E-03
Class I/Class I ND	$N(NH_3)$	4.5E-03
Class I/Class I ND	T_{kin}	5.1E-03
Class II/Class II ND	$NH_3(1,1)$ peak (T_{MB})	3.2E-03
Class II/Class II ND	σ_v	4.0E-03
Class II/Class II ND	$N(NH_3)$	2.7E-06
Class II/Class II ND	T_{kin}	6.8E-03
Class II/Class II ND	$NH_3(2,2)$ peak (T_{MB})	3.9E-03
Class II/Class II ND	$NH_3(3,3)$ peak (T_{MB})	3.5E-03
Both Class I and II/Neither	$NH_3(1,1)$ peak (T_{MB})	8.9E-04
Both Class I and II/Neither	σ_v	1.6E-03
Both Class I and II/Neither	$N(NH_3)$	3.9E-05

3.2.2. Comparison of EGO Subsamples

As discussed in Section 3.1.2, detection rates for the higher-excitation NH_3 transitions differ for various EGO subsamples. We consider seven pairs of EGO subsamples: (1) "likely"/"possible" outflow candidates; (2) sources associated/not associated with IRDCs; (3) H_2O maser detections/nondetections in our survey; (4) Class I CH_3OH maser detections/nondetections (regardless of Class II association); (5) Class II CH_3OH maser detections/nondetections (regardless of Class I association); (6) EGOs associated with only Class I/only Class II CH_3OH masers; and (7) EGOs associated with both Class I and II CH_3OH masers/EGOs associated with neither CH_3OH maser type. To assess whether the NH_3 *properties* of these subsamples exhibit statistically significant differences, we ran two-sided K-S tests of eight parameters: the NH_3 (1,1), (2,2), and (3,3) peaks (T_{MB}), σ_v, $\tau_{(1,1)}$, η_{ff}, $N(NH_3)$, and T_{kin}. To maximize our sample size, we used the parameters from the single-component fits. To check for biases due to sensitivity limits, we also ran two-sided K-S tests of distance and the $NH_3(1,1)$ rms for the same seven pairs of EGO subsamples. Table 5 lists the subsample/parameter combinations that have significantly different distributions, adopting a moderately conservative threshold of <0.01 for the significance of the K-S statistic. Note that K-S tests involving the CH_3OH maser subsamples are limited by small sample sizes, particularly for parameters that require (2,2) or (3,3) detections. While we ran K-S tests in all cases where the subsamples being compared each have $\geqslant 4$ members, we interpret the small-n results with caution. Statistically significant differences are seen most often in the $NH_3(1,1)$ peak temperature, σ_v, the NH_3 column density, and the kinetic temperature. The distributions of these properties for the various subsamples are shown in Figures 7–12.

The most dramatic difference is between the σ_v distributions for EGOs that are/are not detected in H_2O maser emission in our survey (Figure 9). The NH_3 lines are broader toward EGOs associated with H_2O masers, with median σ_v of 1.18 km s^{-1} and 0.80 km s^{-1} for H_2O maser detections and nondetections, respectively ($\sigma v = \mathrm{FWHM}/\sqrt{8 \ln 2}$). This is in agreement with previous single-dish studies of H_2O masers in star-forming regions. In their $NH_3(1,1)$ survey of 164 H_2O masers ($\theta_{FWHP} \sim 1\farcm4$), Anglada et al. (1996) found a correlation between L_{H_2O} and the NH_3 line width; comparing their data with other NH_3 surveys, they found increased NH_3 line widths toward star-forming regions with H_2O masers. Both our results and those of Anglada et al. (1996) are consistent with the H_2O masers being excited in outflows, which also contribute to gas motions in the surrounding clump, increasing the NH_3 line width. Indeed, in high-resolution Karl G. Jansky Very Large Array (VLA) observations of one of the EGOs in our sample, Brogan et al. (2011) detect a hot (220 K), blueshifted outflow component in NH_3 emission, coincident with redshifted H_2O masers. In our survey, EGOs with H_2O masers are also generally found in clumps with higher NH_3 column densities and higher kinetic temperatures than H_2O maser nondetections.

The populations of EGOs associated and not associated with IRDCs show statistically significant differences in three NH_3 properties: $NH_3(1,1)$ peak, σ_v, and the beam filling fraction, η_{ff}. EGOs associated with IRDCs have stronger $NH_3(1,1)$ emission (higher $NH_3(1,1)$ peak temperatures) and narrower NH_3 line widths (Figure 8). We note that the distance distributions for EGOs associated/not associated with IRDCs are statistically indistinguishable based on our K-S tests (K-S significance 0.21, median distance 4.0 and 4.3 kpc, respectively; see also Section 3.2.1). Pillai et al. (2006b) found that IRDCs had, on average, narrower NH_3 line widths than *IRAS*-selected high-mass protostellar objects or UC H II regions. It is perhaps surprising, however, that we see a difference in the line width distributions for IRDC/non-IRDC EGOs, since we are specifically targeting active star-forming regions within IRDCs. The effect may be attributable to emission from more quiescent regions of IRDCs being included within the Nobeyama beam ($73'' \sim 1.4$ pc at a typical distance of 4 kpc). As shown in Figure 13, EGOs associated with IRDCs also generally have larger (though still small, <0.2) beam filling fractions. This is consistent with numerous studies that show NH_3 emission overall follows 8 μm extinction in IRDCs, while exhibiting clumpy substructure (e.g., Pillai et al. 2006b; Devine et al. 2011; Ragan et al. 2011).

Interestingly, there is little evidence for statistically significant differences between the NH_3 properties of "likely" and "possible" outflow candidates. The only properties for which the K-S significance meets our criterion are the $NH_3(1,1)$ and (2,2) peak temperatures. However, the significance values are close to our cutoff (Table 5), and no comparable difference is seen in the distributions of the physical properties ($N(NH_3)$, T_{kin}, etc.). This suggests that the difference in $T_{MB}(1,1)$ and $T_{MB}(2,2)$ might not reflect intrinsic source properties. We find no statistically significant difference between the distance distributions of "likely" and "possible" EGOs. Existing data are insufficient to evaluate other possible effects, such as the peak 4.5 μm positions cataloged by C08 (and so our pointing positions) being systematically further from the driving sources in "possible" EGOs.

EGO subsamples based on CH_3OH maser associations show notable differences in H_2O maser and $NH_3(2,2)$ and (3,3) detection rates (Section 3.1). The K-S test analysis indicates that these CH_3OH maser subsamples also have statistically significant differences in their NH_3 properties (Table 5). EGOs associated with Class I CH_3OH masers (in the study of CE11; Section 3.1.1) have brighter $NH_3(1,1)$ emission (e.g., higher

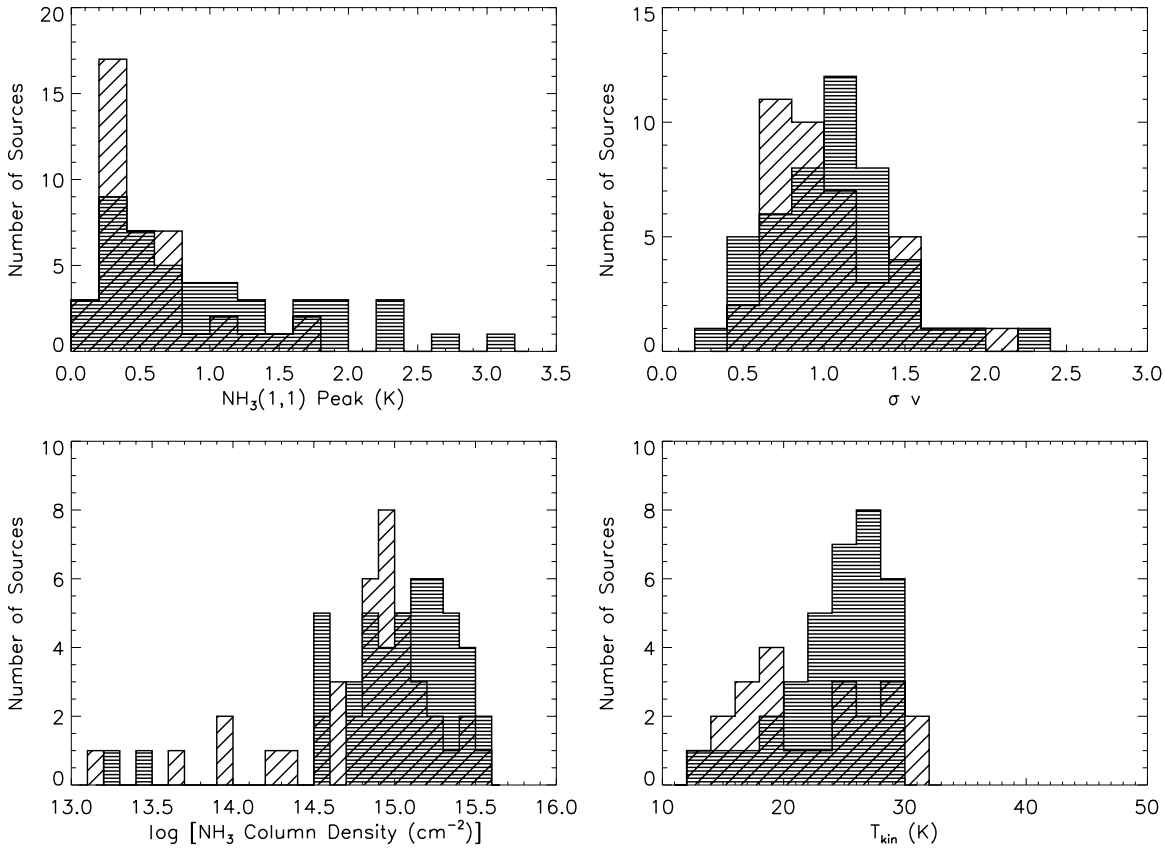

Figure 7. NH_3 property distributions for EGOs classified as "likely" and "possible" MYSO outflow candidates by C08. "Likely" and "possible" sources are plotted as horizontally and diagonally hatched histograms, respectively. Bin sizes are the same as in Figure 4.

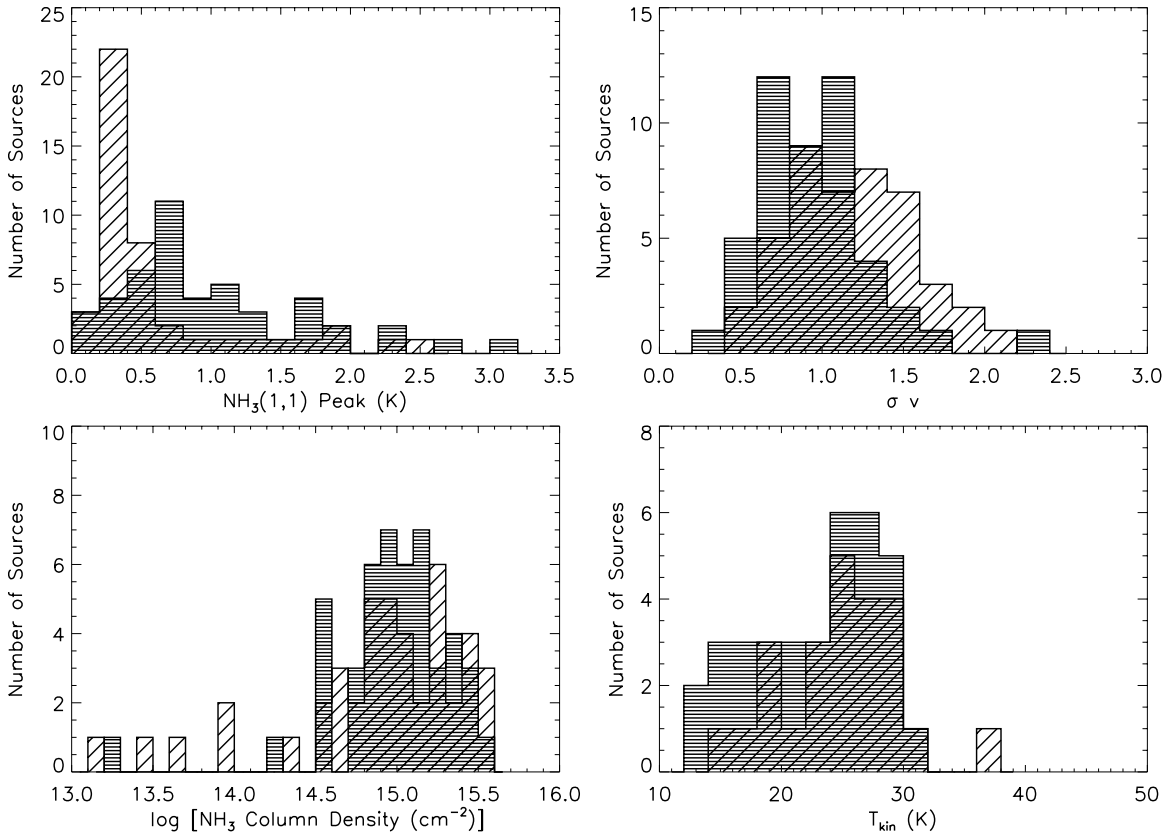

Figure 8. NH_3 property distributions for EGOs associated/not associated with IRDCs, plotted as horizontally and diagonally hatched histograms, respectively. Bin sizes are the same as in Figure 4.

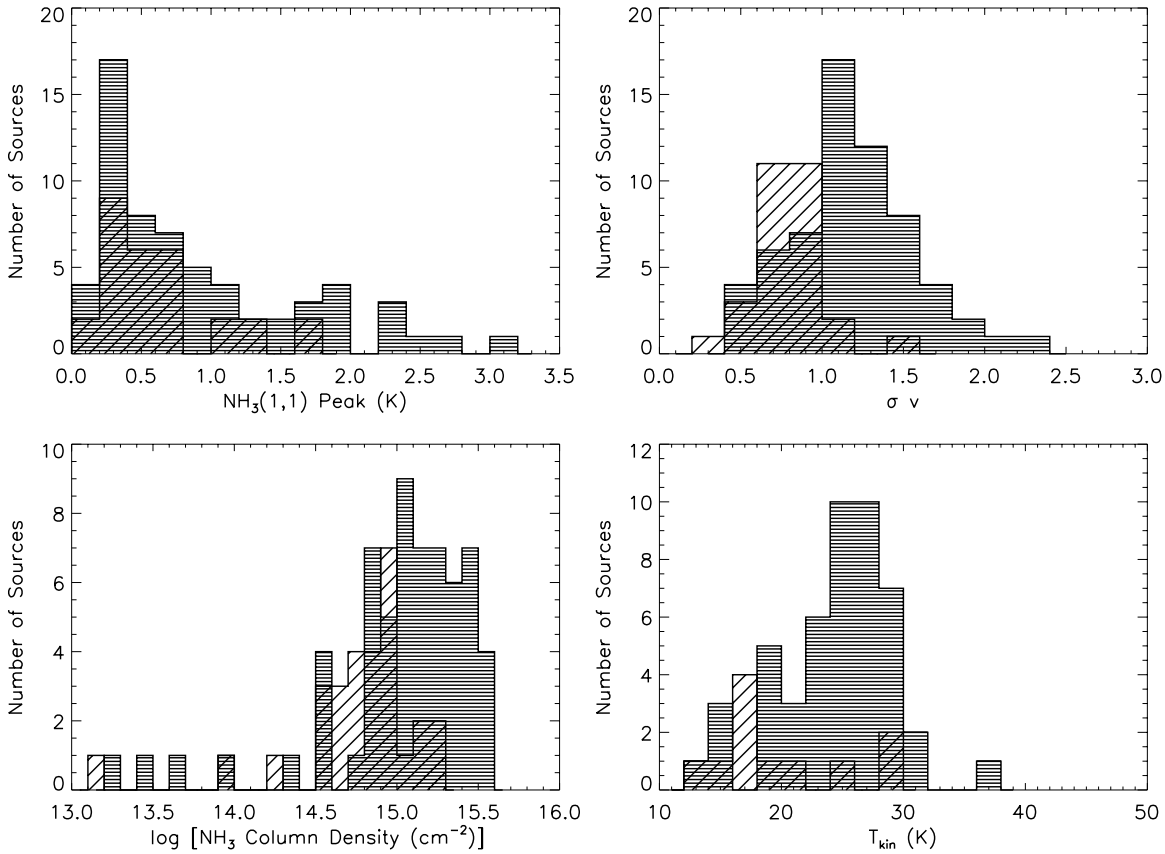

Figure 9. NH_3 property distributions for EGOs that are/are not detected in H_2O maser emission in our survey, plotted as horizontally and diagonally hatched histograms, respectively. Bin sizes are the same as in Figure 4.

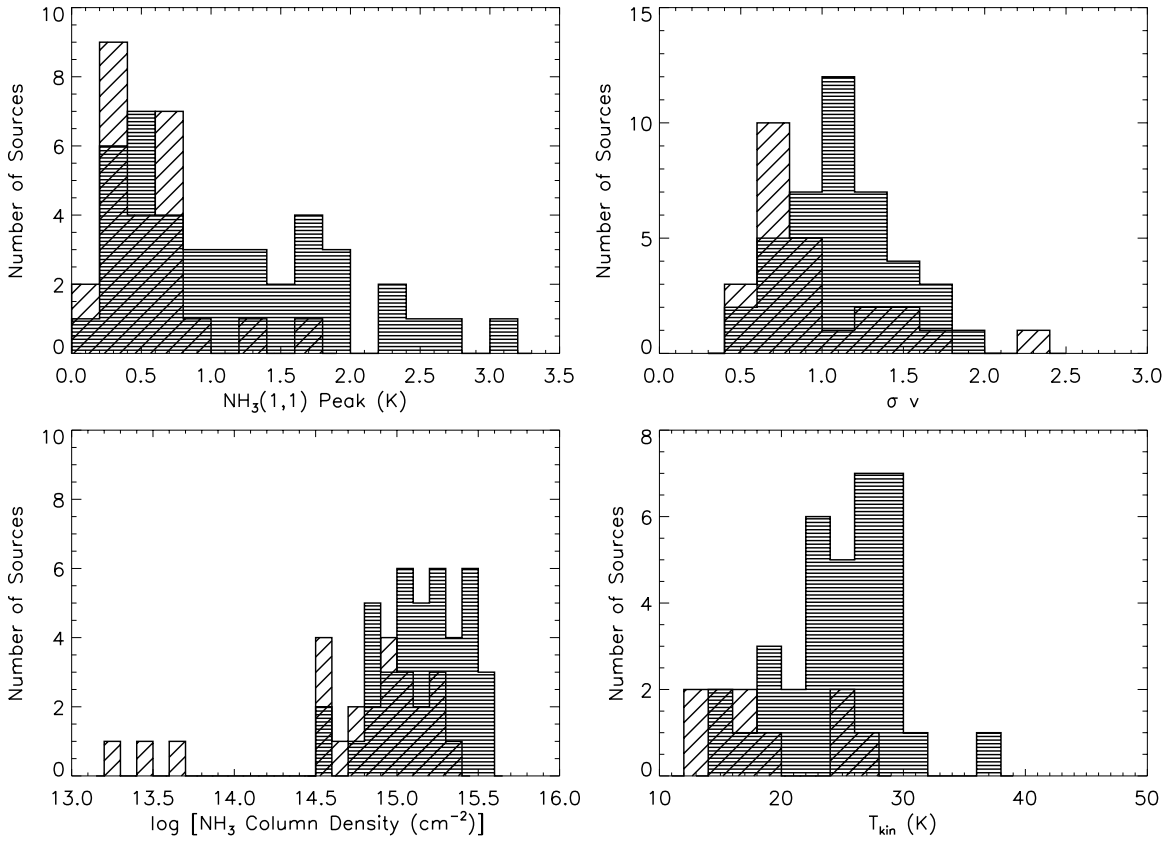

Figure 10. NH_3 property distributions for EGOs that are/are not associated with Class I CH_3OH maser emission (in CE11; see also Section 3.1.1), plotted as horizontally and diagonally hatched histograms, respectively. Bin sizes are the same as in Figure 4.

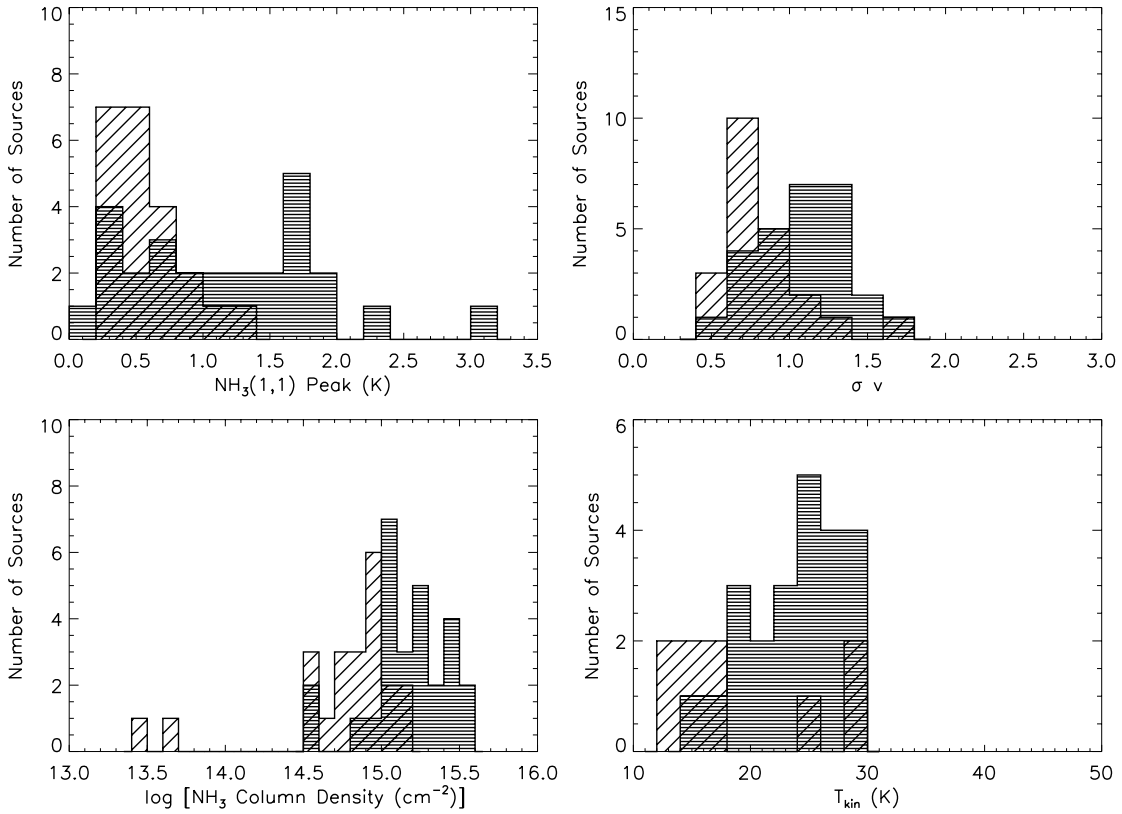

Figure 11. NH_3 property distributions for EGOs that are/are not associated with Class II CH_3OH maser emission (in CE11; see also Section 3.1.1), plotted as horizontally and diagonally hatched histograms, respectively. Bin sizes are the same as in Figure 4.

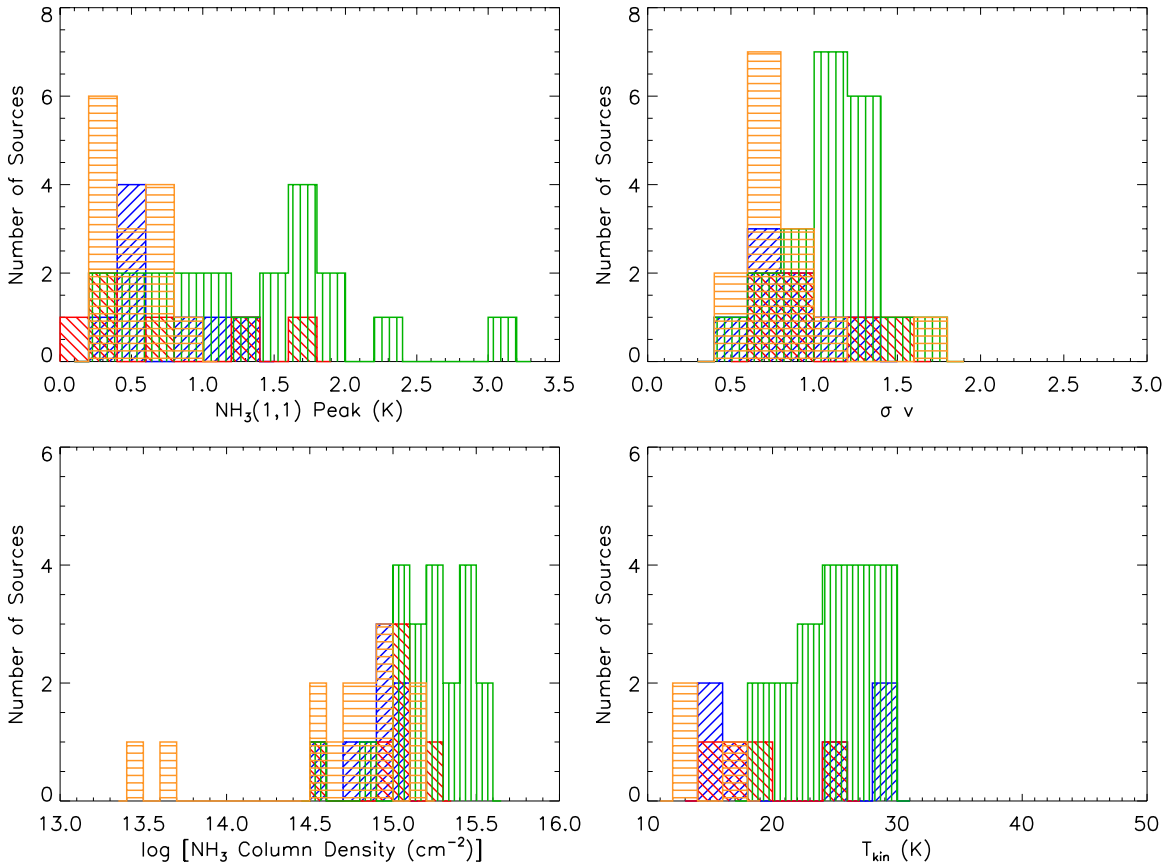

Figure 12. NH_3 property distributions for EGOs associated with both Class I and II CH_3OH masers (green), only Class I CH_3OH masers (blue), only Class II CH_3OH masers (red), and neither type of CH_3OH maser (orange) (CH_3OH maser associations from CE11; see also Section 3.1.1). Bin sizes are the same as in Figure 4.
(A color version of this figure is available in the online journal.)

Table 6
H_2O Maser Properties: Detections

Source Name	σ (Jy)	V_{min} (km s^{-1})	V_{max} (km s^{-1})	V_{peak} (km s^{-1})	V_{range} (km s^{-1})	V_{NH_3} (km s^{-1})	S_{peak} (Jy)	$\int S_\nu dV$ (Jy km s^{-1})	$L_{iso}(H_2O)$ ($L_\odot$)	Notes[a]
G10.29-0.13	0.08	5.3	16.1	12.3	10.8	14.0	0.7	1.548	8.89E-08	BE11
G10.34-0.14	0.11	−13.1	49.8	19.8	62.8	12.0	11.1	64.044	2.45E-06	BE11
G11.92-0.61	0.14	18.2	43.8	39.8	25.6	36.1	53.1	145.844	4.06E-05	HC96, BE11
G12.20-0.03	0.11	47.3	47.6	47.3	0.3	51.2	0.5	0.242	7.62E-07	BE11
G12.42+0.50	0.11	4.5	11.2	5.8	6.7	18.1	2.9	7.828	6.30E-07	...
G12.68-0.18	0.11	8.3	109.7	59.5	101.4	55.7	629.0	1381.320	6.32E-04	BE11
G12.91-0.03	0.11	13.2	16.9	16.7	3.8	56.8	0.7	1.327	6.13E-07	...
G12.91-0.26	0.14	40.4	49.3	40.7	8.9	37.1	1.0	1.010	2.70E-07	*
G14.33-0.64	0.13	14.3	32.3	27.2	18.1	22.5	35.8	108.120	3.12E-06	S10
G14.63-0.58	0.14	21.8	22.6	22.3	0.8	18.6	1.7	1.452	1.00E-07	...

Notes.
[a] References are for previously reported H_2O masers with accurate positions from interferometric observations that fall within the polygonal aperture for the EGO published by C08 (Section 3.3). B02: Beuther et al. (2002). B11: Bartkiewicz et al. (2011). BE11: Breen & Ellingsen (2011). CG11: Caswell & Green (2011). FC99: Forster & Caswell (1999). HC96: Hofner & Churchwell (1996). S10: Sato et al. (2010). W06: Wang et al. (2006). "· · ·" indicates no H_2O maser reference meeting these criteria was found in a SIMBAD search.
* "Outflow-only" source in C08. The published polygonal aperture does not include the "central" source, which is associated with H_2O maser emission (G12.91-0.26; G34.26+0.15; G37.55+0.20: Breen & Ellingsen 2011; Forster & Caswell 1999; Beuther et al. 2002, respectively).
(This table is available in its entirety in a machine-readable form in the online journal. A portion is shown here for guidance regarding its form and content.)

NH_3(1,1) peak temperatures), broader NH_3 line widths, and higher NH_3 column densities and kinetic temperatures than Class I CH_3OH maser nondetections (Figure 10). Class II CH_3OH maser detections/nondetections show the same trends in the same properties (Figure 11). EGOs associated with both Class I and II CH_3OH masers likewise show stronger NH_3(1,1) emission and increased NH_3 line widths and column densities compared to EGOs associated with neither type of CH_3OH maser. Too few EGOs with neither CH_3OH maser association are detected in NH_3(2,2) to run a K-S test on T_{kin}, but Figure 12 shows that the kinetic temperature is indeed also higher toward EGOs with Class I and II CH_3OH masers. Of the CH_3OH maser subsamples, the most significant difference (lowest K-S significance) is between the $N(NH_3)$ distributions for EGOs with/without Class II CH_3OH masers.

The majority of our sample of Class II CH_3OH maser detections (21/28), and about half of our sample of Class I CH_3OH maser detections (21/41), are comprised of EGOs associated with both Class I and II CH_3OH masers. Similarly, the majority of the Class II nondetections (15/23) and ∼1/2 the Class I nondetections (15/28) are EGOs with neither type of CH_3OH maser. Thus, it is not surprising that the Class I detection/nondetection, Class II detection/nondetection, and both (Class I and II)/neither EGO subsamples show similar patterns in their NH_3 properties. The sample sizes of EGOs known to be associated with *only* Class I or *only* Class II CH_3OH masers are small (Table 2). Nonetheless, there are no indications of systematic differences in the NH_3 properties of Class I-only and Class II-only EGOs, either in the K-S test results or in the plots shown in Figure 12.

3.3. Water Maser Properties

For each EGO with detected H_2O maser emission in our survey, Table 6 lists the rms, peak flux density, velocity of peak maser emission, minimum and maximum velocities of maser emission (>4σ; see also Section 3.1.1), integrated flux density, and isotropic maser luminosity. Spectra are presented in Figure 14 (available online in its entirety), with the minimum and maximum velocities of detected maser emission plotted as dotted lines. In the absence of precise positions, the extreme variability of H_2O masers makes it very difficult to establish with confidence whether or not a newly observed maser is identifiable with one previously reported (as discussed in Breen & Ellingsen 2011, and references therein). The present study is, to our knowledge, the first systematic search for H_2O maser emission toward EGOs. We note in Table 6 H_2O masers detected in high-resolution studies targeting other samples that fall within the polygonal EGO apertures from C08, but do not attempt to correlate our Nobeyama spectra with previous single-dish detections. As in similar studies (e.g., Anglada et al. 1996; Urquhart et al. 2011), we estimate the isotropic H_2O maser luminosity, $L(H_2O)$, as

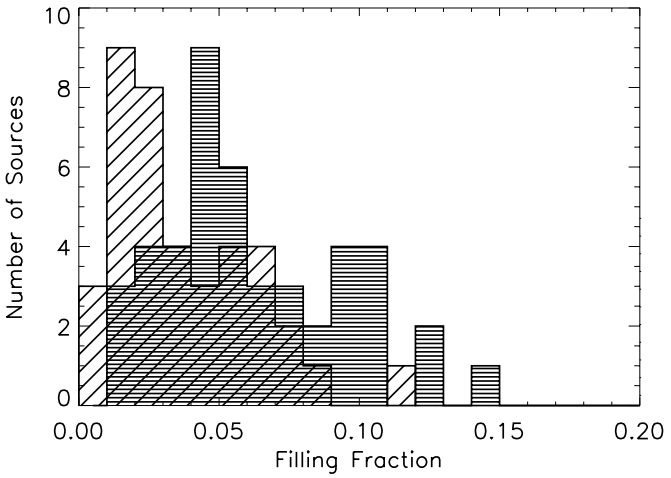

Figure 13. Distribution of the beam filling fraction, η_{ff}, for EGOs associated/not associated with IRDCs, plotted as horizontally and diagonally hatched histograms, respectively. The bin size is 0.01. Sources for which $T_{ex} = T_{kin}$ and $\eta_{ff} = 1$ are not shown.

$$\left[\frac{L(H_2O)}{L_\odot}\right] = 2.30 \times 10^{-8}\left[\frac{\int S_\nu dV}{\text{Jy km s}^{-1}}\right]\left[\frac{D}{\text{kpc}}\right]^2, \quad (3)$$

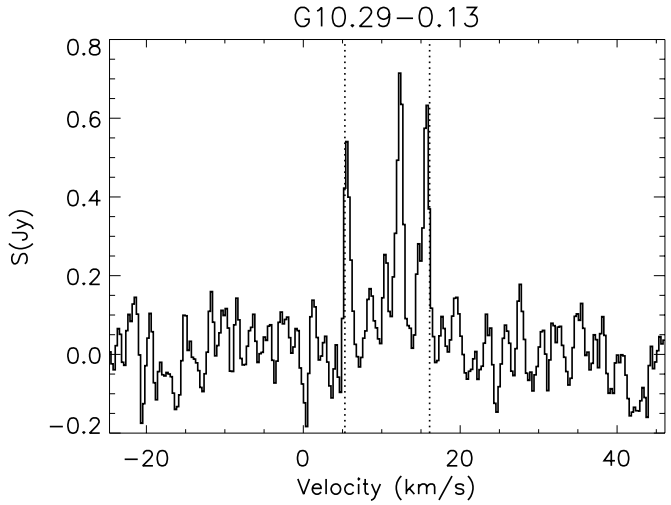

Figure 14. H_2O maser spectrum. The minimum and maximum velocities of detected maser emission (>4σ; Table 6) are shown as dotted vertical lines. The velocity range shown for each EGO extends from $V_{\rm min,water} - 30\,{\rm km\,s^{-1}}$ to $V_{\rm max,water} + 30\,{\rm km\,s^{-1}}$.

(An extended version of this figure is available in the online journal.)

where D is the distance to the source (Section 3.2.1, Table 3) and $\int S_\nu dV \sim \sum_i (S_i \Delta v_i)$ is calculated over all channels that meet our 4σ detection criterion. For H_2O maser nondetections, Table 7 lists the rms and upper limit for the isotropic H_2O maser luminosity (calculated from Equation (3) for 4σ and two channels). The distributions of H_2O maser peak and integrated flux densities, luminosity, and velocity range for H_2O maser detections in our sample are shown in Figure 15.

3.3.1. High-velocity Features

H_2O masers are known for their wide velocity ranges and high-velocity features, as compared to other masers found in MSFRs (e.g., CH_3OH and OH). The velocity of the strongest H_2O maser emission in a given source is nonetheless generally well correlated with the $v_{\rm LSR}$ of the dense gas (e.g., Churchwell et al. 1990; Anglada et al. 1996; Urquhart et al. 2011). Notably, for the Red *MSX* Source (RMS)[15] sample of MIR-bright MYSOs and UC H II regions, the distribution of $V_{\rm H_2O,peak} - V_{\rm NH_3}$ is skewed toward negative velocities. The offset (from zero) is statistically significant, and indicates that blueshifted masers are stronger and more prevalent than redshifted masers (Urquhart et al. 2011). In our sample of 62 sources detected in both H_2O maser and $NH_3(1,1)$ emission, the mean offset $V_{\rm H_2O,peak} - V_{\rm NH_3}$ is $-2.43\,{\rm km\,s^{-1}}$ and the median offset $-0.54\,{\rm km\,s^{-1}}$. However, in our (smaller) sample, the offset from zero is not statistically significant (standard errors 1.37 and 1.72, respectively). The distribution of $V_{\rm H_2O,peak} - V_{\rm NH_3}$ for our EGO sample is shown in Figure 16.

The relative frequency of blueshifted and redshifted emission can also be accessed by examining high-velocity maser features (generally defined as $V - V_{\rm LSR} \geqslant 30\,{\rm km\,s^{-1}}$, e.g., Caswell & Breen 2010; Urquhart et al. 2011). Caswell & Breen (2010) recently analyzed high-velocity emission in numerous H_2O

[15] For additional details on the RMS sample, see Hoare et al. (2005); Urquhart et al. (2008).

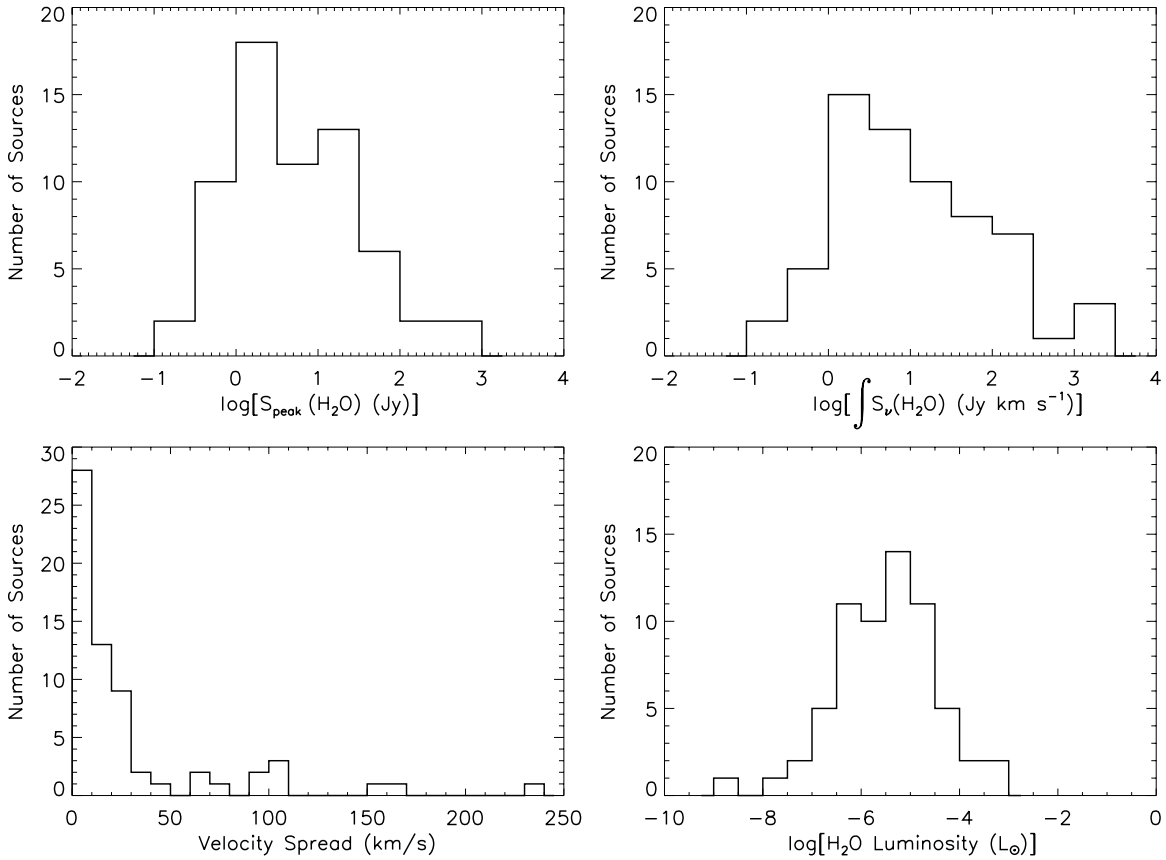

Figure 15. Histograms showing the distributions of H_2O maser properties for all H_2O maser detections in our sample. The panels show (clockwise from upper left): peak flux density, integrated flux density, isotropic H_2O maser luminosity, and velocity range of maser emission (>4σ) (Section 3.3). Bin sizes are 0.5 dex (peak and integrated flux densities and luminosity) and $10\,{\rm km\,s^{-1}}$ (velocity range).

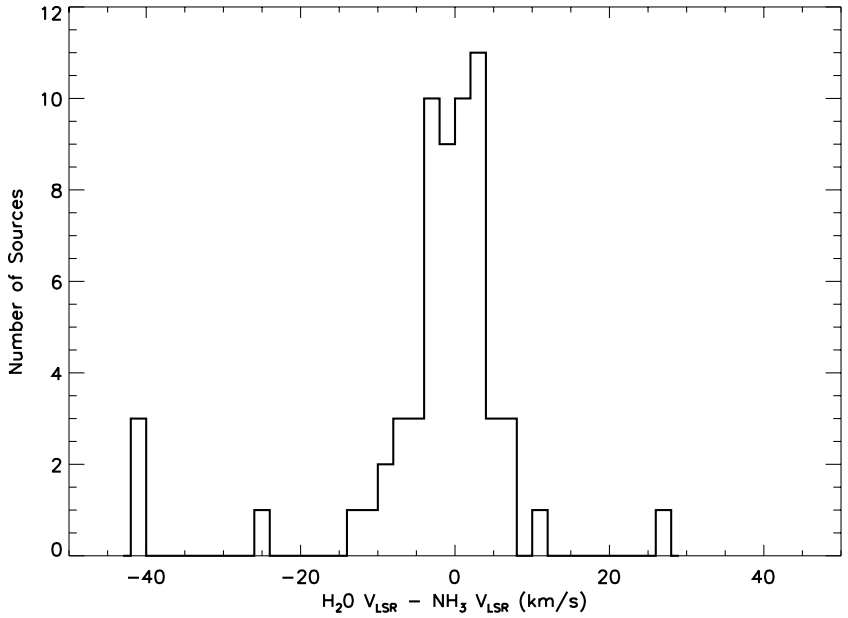

Figure 16. Distribution of the difference between the NH_3 v_{LSR} and the velocity of peak H_2O maser emission for all sources with both H_2O maser and NH_3(1,1) detections. The bin size is 2 km s^{-1}.

Table 7
H_2O Maser Nondetections: Limits

Source Name	σ (Jy)	$L_{iso}(H_2O)$[a] ($L_\odot$)
G11.11-0.11	0.14	<1.09E-06
G12.02-0.21	0.10	<1.41E-07
G16.58-0.08	0.10	<5.04E-08
G16.61-0.24	0.10	<5.68E-08
G19.36-0.03	0.16	<3.40E-08
G21.24+0.19	0.10	<1.89E-08
G24.11-0.17	0.09	<9.87E-08
G24.11-0.18	0.10	<1.09E-07
G28.28-0.36	0.17	<8.07E-08
G28.83-0.25	0.17	<2.01E-07
G28.85-0.23	0.12	<1.73E-07
G29.84-0.47	0.14	<1.09E-07
G29.89-0.77	0.16	<1.74E-07
G29.91-0.81	0.17	<1.87E-07
G29.96-0.79	0.06	<6.52E-08
G35.04-0.47	0.12	<5.82E-08
G35.83-0.20	0.13	<2.10E-08
G36.01-0.20	0.10	<1.50E-07
G40.28-0.27	0.08	<8.94E-08
G40.60-0.72	0.10	<9.26E-08
G44.01-0.03	0.10	<1.16E-07
G48.66-0.30	0.16	<4.68E-08
G49.27-0.32	0.15	<2.18E-07
G54.11-0.04	0.16	<1.09E-07
G54.11-0.05	0.11	<7.35E-08
G56.13+0.22	0.06	<6.80E-08
G57.61+0.02	0.11	<1.11E-07
G58.09-0.34	0.06	<1.69E-09
G58.79+0.63	0.07	<6.48E-08
G62.70-0.51	0.06	<4.15E-08

Note. [a] All limits are 4σ.

maser subsamples and proposed that an excess of sources showing only blueshifted high-velocity emission is an indicator of youth. For H_2O masers associated with Class II CH_3OH but not OH masers (from the sample of Breen et al. 2010a), they find a "blue" (blueshifted high-velocity emission only) fraction of 16%, a "red" fraction of 8%, and a "red+blue" (both blueshifted and redshifted high-velocity H_2O maser features) fraction of 7%. Interestingly, Urquhart et al. (2011) find a similar ratio of "blue":"red" sources in their much larger sample of RMS YSOs and UC H II regions, though a smaller overall fraction (22%) of their detected H_2O masers show some high-velocity emission. Twelve of our EGO targets (∼19%) have high-velocity H_2O maser features (offset by $\geqslant$30 km s^{-1} from the NH_3 v_{LSR}): 6 "blue," 1 "red," and 5 "red+blue." Of these 12 EGOs, 5 are associated with both Class I and II CH_3OH masers, 4 are associated with Class I CH_3OH masers and are classified as Class II "no information" in CE11, 1 is associated with Class I but not Class II CH_3OH masers, and 2 are not included in CE11. Our sample sizes and those of Caswell & Breen (2010) are too small to warrant detailed comparisons; however, the "blue":"red" excess we observe is generally consistent with their results for CH_3OH maser sources.

3.3.2. Comparison of EGO Subsamples

To look for differences in the properties of H_2O masers associated with the various EGO subsamples, we ran two-sided K-S tests for four parameters: velocity range, peak flux density, integrated flux density, and isotropic maser luminosity. The subsample pairs considered were the same as outlined above (Section 3.2.2), with the exception of H_2O maser detections/nondetections (since we are investigating H_2O maser properties, only detections are considered). We find no evidence for statistically significant differences. As an example, Figures 17 and 18 show histograms of the H_2O maser luminosity, shaded by subsample, for the six subsample pairs.

3.4. Properties of Associated Dust Clumps

Of the 94 northern EGOs in our survey, 82 fall with the coverage of the 1.1 mm BGPS (resolution 33″; Aguirre et al. 2011; Rosolowsky et al. 2010), and 77 are associated with BGPS

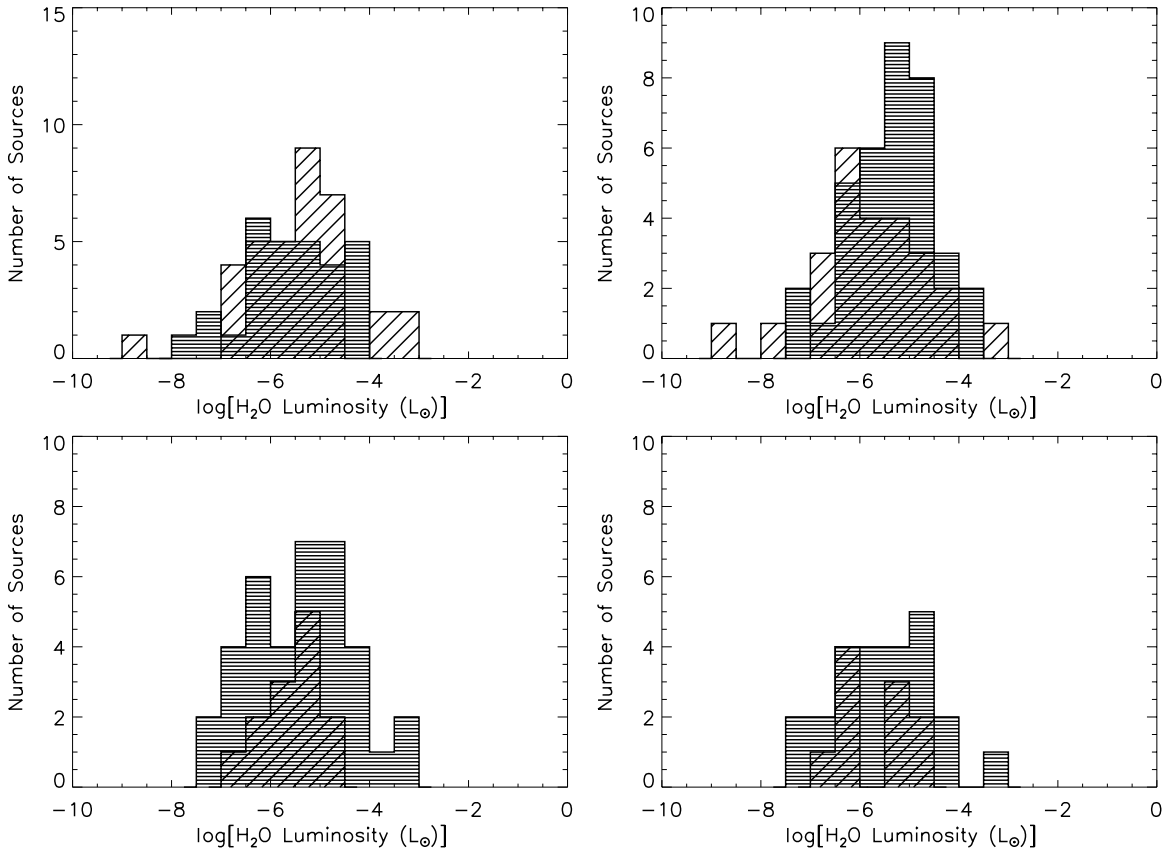

Figure 17. Distributions of the H_2O maser luminosity for different EGO subsamples. Upper left: divided by association with IRDCs. EGOs associated and not associated with IRDCs are plotted as horizontally and diagonally hatched histograms, respectively. Upper right: divided by "likely"/"possible" outflow candidates. EGOs classified as "likely" and "possible" by C08 are plotted as horizontally and diagonally hatched histograms, respectively. Lower left: divided by Class I CH_3OH maser association (regardless of Class II association/information). Class I detections/nondetections are plotted as horizontally and diagonally hatched histograms, respectively. Lower right: divided by Class II CH_3OH maser association (regardless of Class I association). Class II detections/nondetections are plotted as horizontally and diagonally hatched histograms, respectively. The bin size is 0.5 dex, as in Figure 15. The significance of the K-S statistic (low values indicate different cumulative distribution functions) is 0.98 (IRDC/no IRDC), 0.06 (likely/possible), 0.51 (Class I/no Class I), and 0.51 (Class II/no Class II), indicating no statistically significant differences in the distributions of the H_2O maser luminosities.

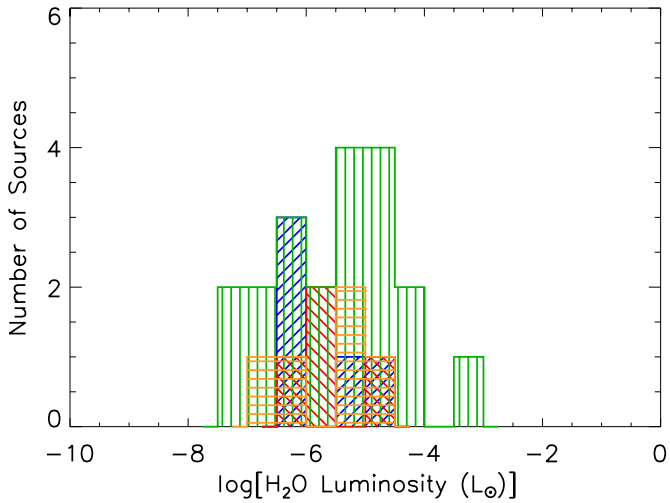

Figure 18. Distribution of H_2O maser luminosity for EGOs associated with both Class I and II CH_3OH masers (green), only Class I CH_3OH masers (blue), only Class II CH_3OH masers (red), and neither type of CH_3OH maser (orange). The bin size is 0.5 dex.

(A color version of this figure is available in the online journal.)

sources.[16] The BGPS source extraction algorithm, Bolocat, uses a seeded watershed approach to identify the boundaries of BGPS sources, and outputs "label maps" in which each pixel assigned to a source has a value of that source's BGPS catalog number (see Rosolowsky et al. 2010; Dunham et al. 2011a, for more details). If the position of an EGO from C08 falls within the Bolocat-defined boundary of a BGPS source, we consider the EGO and BGPS source to be associated.

We calculate clump gas masses from the 1.1 mm dust continuum emission

$$M_{\rm gas} = \frac{4.79 \times 10^{-14} R S_\nu({\rm Jy}) D^2({\rm kpc})}{B(\nu, T_{\rm dust})\kappa_\nu}, \quad (4)$$

where S_ν is the integrated flux density from the BGPS catalog corrected by the recommended factor of 1.5 ± 0.15 (Aguirre et al. 2011; Dunham et al. 2010), D is the distance to the source (Section 3.2.1, Table 3), $B(\nu, T_{\rm dust})$ is the Planck function, R is the gas-to-dust mass ratio (assumed to be 100), and κ_ν is the dust mass opacity coefficient in units of cm^2 g^{-1}. We follow recent BGPS studies (e.g., Dunham et al. 2010,

[16] The slight difference from the statistics in Dunham et al. (2011a) is because we consider G19.01−0.03 as a single EGO, while they treat this EGO and its northern and southern outflow lobes (for which separate photometry is given in C08) as three objects.

Table 8
Properties of Associated BGPS Dust Clumps[a]

Source Name	BGPS Cat. ID	$S_{1.1\,mm}$[d] (Jy)	Distance[e] (kpc)	Radius ($''$)	Radius (pc)	Single Component[b] Clump Mass ($M_\odot$)	Single Component[b] Log(n_{H_2}) (Log(cm^{-3}))	Two Component[c] Clump Mass ($M_\odot$)	Two Component[c] Log(n_{H_2}) (Log(cm^{-3}))
G10.29−0.13	1474	9.4(0.7)	1.58(+0.86, −1.13)	68.1	0.52	427^{+774}_{-398}	$4.1^{+6.2}_{-4.1}$	585	4.2
G10.34−0.14	1483	8.6(0.6)	1.29(+0.92, −1.23)	84.9	0.43	179^{+441}_{-179}	$3.7^{+8.2}_{-3.7}$	361	4.0
G11.11−0.11	1589	2.3(0.2)	12.67(+0.48, −0.41)[f]	56.7	4.18	11740^{+3341}_{-2679}	$3.1^{+2.7}_{-2.6}$	7967	2.9
G12.02−0.21	1668	1.0(0.1)	5.30(+0.20, −0.20)[g]	38.0	1.75	$>1024^{+361}_{-292}$	$>3.7^{+3.4}_{-3.2}$	...	...
G12.20−0.03	1682	2.1(0.2)	11.70(+0.31, −0.27)[f]	52.8	3.86	5732^{+1674}_{-1373}	$3.0^{+2.5}_{-2.4}$	...	...

Notes.
[a] Properties calculated as described in Section 3.4 using nominal distances from Table 3. For EGOs matched to a BGPS source but undetected in NH_3 emission, the BGPS clump ID and radius are listed, but no clump mass and density are calculated. Uncertainties in n_{H_2} are also in units of log(cm^{-3}).
[b] Calculated from the integrated flux density in the BGPS catalog assuming isothermal dust emission and $T_{dust} = T_{kin}$ from Table 3. Quoted ranges include the uncertainties in the integrated flux density from the BGPS catalog, the recommended BGPS flux correction factor, and the distance. See also Sections 3.4 and 4.1.2.
[c] Calculated for sources fit with two NH_3 components as described in Section 3.4. Because the systematic uncertainties in this estimate are difficult to quantify, only nominal values are listed (which assume a BGPS correction factor of 1.5 and the nominal integrated flux from the BGPS catalog).
[d] Integrated flux density taken directly from the BGPS catalog, Rosolowsky et al. (2010). The recommended correction factor is applied when calculating clump masses and densities (Section 3.4).
[e] These data are identical to those in Table 3, and are duplicated here for convenience.
[f] Associated with a 6.7 GHz CH_3OH maser assigned the far distance by Green & McClure-Griffiths (2011). Except for G12.20−0.03 and G45.80−0.36, all far distance assignments are "B" classifications in their scheme (see also Section 3.2.1). We adopt the far kinematic distance estimated from the NH_3 v_{LSR}.
[g] The longitude and velocity of this source indicate that it is likely in the near 3 kpc arm (see, for example, Figure 1 of Green et al. 2009). Following Green & McClure-Griffiths (2011), we place this source on a circle of radius 3.4 kpc around the Galactic Center, and adopt a distance uncertainty of ±0.2 kpc.
[h] It is unclear if this source is at the near or the far distance (e.g., Cyganowski et al. 2011a; Green & McClure-Griffiths 2011).
[i] Maser parallax distance. References: G23.01−0.41, Brunthaler et al. (2009). G34.39+0.22 and G34.41+0.24: Kurayama et al. (2011).
[j] NH_3 nondetection. G49.42+0.33: distance estimated using $H^{13}CO^+$ velocity from C09. G53.92−0.07: distance estimated using H_2O maser peak velocity. G57.61+0.02: distance estimated from velocity of weak (3.9σ) NH_3(1,1) emission below our 4σ detection threshold. See also Section 3.2.1.
[k] The density range is not constrained because the lower end of the distance range is 0.0 kpc.

(This table is available in its entirety in a machine-readable form in the online journal. A portion is shown here for guidance regarding its form and content.)

2011a, 2011b) in adopting $\kappa_{271\,GHz}/R = 0.0114\,cm^2\,g^{-1}$. Our NH_3 observations provide a measurement of the clump-scale gas kinetic temperature, T_{kin}, and we assume $T_{dust} = T_{kin}$ in calculating the clump masses. To estimate the volume-averaged number densities of the clumps, we use the clump gas mass from Equation (4) and the deconvolved angular source radius from the BGPS catalog (Rosolowsky et al. 2010), assuming spherical geometry. For consistency with Hill et al. (2005; see Section 4.2), we adopt a mean mass per particle $\mu = 2.29\,m_H$. The 1.1 mm flux densities, radii, gas masses, and volume-averaged number densities for the clumps associated with our target EGOs are listed in Table 8. For the three BGPS sources in our sample that could not be stably deconvolved (listed as "null" radii in the BGPS catalog), we adopt half the BGPS beam size as an upper limit to the source radius, e.g., $R < 16''.5$. The derived number densities for these sources are thus lower limits, and are indicated as such in the tables and figures. We regard this radius upper limit as conservative because source radii can sometimes be determined for source diameters smaller than a beam width. However, given the substantial uncertainty in relating an emission distribution to a true radius, particularly at low signal-to-noise ratio, a more aggressive limit could be incorrect (e.g., Rosolowsky et al. 2010; Rosolowsky & Leroy 2006). If we instead adopted an upper limit of half the BGPS beam size for the source diameter, this would increase the density limits by a factor of eight.

To estimate clump parameters consistently for the largest possible number of sources in our sample, we first calculate M_{gas} and n_{H_2} as described above using the gas kinetic temperatures derived from the single-component NH_3 fitting. For EGOs undetected in NH_3(2,2), we treat the best-fit T_{kin} as an upper limit (see also Section 3.2); the derived clump mass and density are thus lower limits. The clump masses estimated using well-determined kinetic temperatures are in the range of hundreds to thousands of solar masses (Figure 19), with a mean (median) of ∼1850 $M_\odot$ (∼1010 $M_\odot$). The range of EGO dust clump masses is consistent with expectations for MYSOs based on bolometer studies of other samples. For example, Rathborne et al. (2006) find a median IRDC mass of ∼940 $M_\odot$

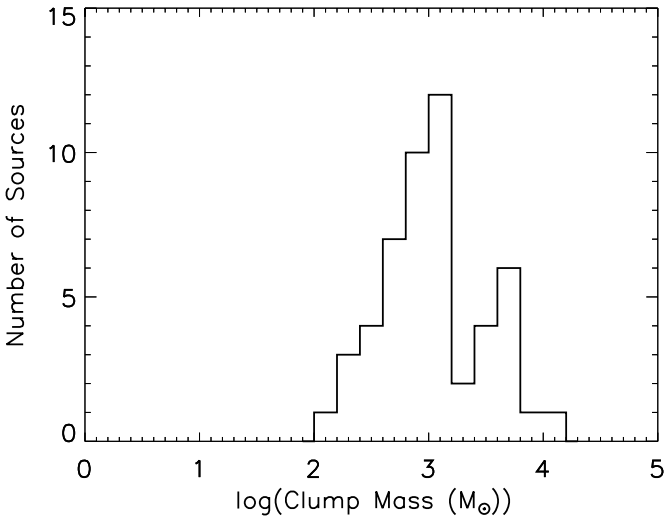

Figure 19. Distribution of clump masses estimated from 1.1 mm dust continuum emission for sources with well-determined kinetic temperatures (Section 3.4). For clarity, only nominal mass values from Table 8 are plotted. The bin size is 0.2 dex.

(range ∼120 to 16,000 $M_\odot$), and Mueller et al. (2002) report a similar range and a mean mass of 2020 $M_\odot$ for a sample of H_2O maser sources with high luminosities ($L_{bol} > 10^3\ L_\odot$). The star-forming sources (those with Class II CH_3OH masers and/or UC H II regions) in the Hill et al. (2005) dust clump sample similarly span a mass range of $\sim 10^2$–$10^4\ M_\odot$ (Hill et al. 2010). Only one EGO appears to be a potential example of a nearby, low-mass YSO based on the properties of its associated dust clump: G49.91+0.37, which has a low ($<10\ M_\odot$) lower-limit mass and a near kinematic distance of $0.53\ ^{+0.52}_{-0.53}$ kpc.

The significantly improved fits obtained with two temperature components for ∼1/4 of our NH_3 spectra indicate emission from both warmer inner regions and cooler outer envelopes along our lines of sight. As noted in Section 2.2, the beam filling factor η_{ff} and the excitation temperature T_{ex} are degenerate for the two-component modeling. To estimate the relative contributions of the warm and cool components, we assume $T_{kin} = T_{ex}$ and calculate $\eta_{ff} = (T_{ex} - 2.73)/(T_{kin} - 2.73)$ for each component. We then assign weights, $W_{warm} = 1/((\eta_{cool}/\eta_{warm}) + 1)$ and $W_{cool} = 1/((\eta_{warm}/\eta_{cool}) + 1)$, and recalculate the clump mass as $M_{total} = M_{gas,warm} + M_{gas,cool}$ where

$$M_{gas,warm} = \frac{4.79 \times 10^{-14} R S_\nu(\mathrm{Jy}) W_{warm} D^2(\mathrm{kpc})}{B(\nu, T_{dust,warm})\kappa_\nu} \quad (5)$$

and

$$M_{gas,cool} = \frac{4.79 \times 10^{-14} R S_\nu(\mathrm{Jy}) W_{cool} D^2(\mathrm{kpc})}{B(\nu, T_{dust,cool})\kappa_\nu}. \quad (6)$$

The volume-averaged number density is then estimated as described above, using M_{total} in place of the single-temperature isothermal gas mass calculated from Equation (4). We can estimate revised clump masses and number densities in this way for 16 of the 21 sources with two-component NH_3 fits. For these sources, the median(mean) mass fraction in the warm component is 5.5%(10.0%). For five sources with two-component fits, $T_{ex} = T_{kin}$ for one of the modeled temperature components (the upper limit). Coincidentally, three of these five sources fall outside the BGPS survey area. For the remaining two sources, we retain the isothermal masses and densities in our analysis.

3.4.1. BGPS 1.1 mm Nondetections

Young, actively accreting MYSOs are expected to be still embedded in their natal clumps; as discussed above, we find a strong correlation between EGOs and BGPS 1.1 mm dust sources. The five EGOs within the BGPS survey area but not matched to a BGPS source are all detected in $NH_3(1,1)$ emission; as a group, they are not particularly distant (all have $D < 5.5$ kpc, Table 3). The $NH_3(1,1)$ detections indicate that dense gas is present; here we briefly consider the nature of these EGOs and the reasons for their lack of counterparts in the BGPS catalog.

The rms noise of the BGPS varies with Galactic longitude, and is locally increased in the vicinity of bright sources (Aguirre et al. 2011). Two of the unmatched EGOs (G62.70−0.51 and G58.09−0.34) are at $l \sim 60°$, where the noise is significantly higher than in most of the inner Galaxy (Figure 11 of Aguirre et al. 2011); G62.70−0.51 is also near the edge of the BGPS map. A third unmatched EGO, G49.27−0.32, is in a region of locally high noise due to its proximity to W51. Thus, it is possible that these EGOs are associated with mm dust clumps that would have been detected elsewhere in the BGPS. The distances of G49.27−0.32 and G62.70−0.51 are typical of our sample ($D = 5.5$ and 3.9 kpc, respectively, Table 3), and their properties are generally consistent with those of EGOs detected only in $NH_3(1,1)$ emission and matched to BGPS sources. The increased noise of the BGPS at the locations of these EGOs thus seems to be a likely explanation for their lack of BGPS counterparts. G58.09−0.34, however, may be an example of a nearby, low-mass YSO: it has a near kinematic distance of $0.74^{+0.65}_{-0.61}$ kpc and exceptionally narrow $NH_3(1,1)$ emission ($\sigma v \sim 0.23$ km s^{-1}).

Examining the BGPS images suggests that the two other unmatched EGOs (G50.36−0.42 and G29.89−0.77) are associated with 1.1 mm emission, despite not being matched to BGPS catalog sources. G50.36−0.42 appears to be associated with faint 1.1 mm emission that fell below the threshold for extraction as a BGPS source (Rosolowsky et al. 2010). A C08 "possible" outflow candidate ($D = 3.0$ kpc), G50.36−0.42 also has detected H_2O maser emission in our survey. G29.89−0.77 is immediately adjacent to a BGPS source, but the C08 position falls outside the BGPS source boundary defined by the label maps. Also a C08 "possible" outflow candidate, G29.89−0.77 has the strongest NH_3 emission of the unmatched EGOs; though the (2, 2) line is formally undetected by our 4σ criterion, weak $NH_3(2,2)$ emission is evident in the spectrum. Taken together, this evidence suggests G29.89−0.77 and G50.36−0.42 are likely similar in nature to EGOs that are matched to BGPS sources.

4. DISCUSSION

4.1. EGOs in Context

4.1.1. Comparison with Other Samples

A notable feature of EGOs, compared to other samples of young massive (proto)stars, is their very strong association with both Class I and II CH_3OH masers, reflected in remarkably high detection rates in CH_3OH maser surveys to date (e.g., C09, CE11). Since H_2O maser and NH_3 observations are common tools for studying massive star formation, our Nobeyama survey allows us to better place EGOs in their broader context, by comparing their molecular environments to those of MYSOs selected using other criteria/tracers. Table 9 summarizes H_2O maser and $NH_3(1,1)$ detection rates toward a variety of MYSO samples from the literature, chosen to cover a range of sample selection criteria, survey parameters, and proposed evolutionary state of the target objects. The strong correlation of EGOs with 6.7 GHz CH_3OH masers and with dust clumps (Section 3.4) suggests these as natural comparison samples (indeed, the samples of Breen & Ellingsen 2011 and of Bartkiewicz et al. 2011 include some EGOs; see also discussion therein). "Active" IRDC cores in Chambers et al. (2009) are defined by the presence of "green fuzzy" and 24 μm emission. They define "green fuzzy" broadly, compared to C08 EGOs; still, one might expect these sources to be similar to EGOs associated with IRDCs. In contrast, MYSO and UC H II samples compiled using the *IRAS* or *MSX* point-source catalogs comprise sources that are brighter than EGOs in the MIR and so likely more luminous and/or more evolved (see also C08).

As illustrated by Table 9, H_2O maser detection rates toward massive (proto)star samples span a broad range, from <20% to >80%: our overall detection rate of 68% is toward the upper end of this range. Notably, our H_2O maser detection rate toward EGOs associated with both Class I and II CH_3OH

Table 9
H_2O Maser and NH_3 Surveys of MYSO Samples: Detection Rate Comparison

Sample	Reference[a]	H_2O Maser			$NH_3(1,1)$		
		Sensitivity	Resolution[b]	Detection Rate	Sensitivity	Resolution[b]	Detection Rate
EGOs (overall)[c]	this work	$\sigma \sim 110$ mJy	SD (73″)	68%	$\sigma \sim 50$ mK	SD (73″)	97%
EGOs (IRDC)[c]				62%			100%
EGOs (Class I CH_3OH)[c]				90%			100%
EGOs (Class II CH_3OH)[c]				86%			96%
EGOs (Class I and II CH_3OH)[c]				95%			100%
EGOs (Neither CH_3OH)[c]				33%			93%
Dust Clumps (overall)[d]	BE11/H10	$\sigma \sim 30$–40 mJy	Int. ($\sim 2''$)	44%	variable	SD (52″)	56%
Dust Clumps (mm only)[d]	BE11/H10			23%			53%
Dust Clumps (Class II CH_3OH)[d]	BE11/H10			79%			65%
Dust Clumps (Class II CH_3OH & cm cont.)[d]	BE11/H10			83%			50%
Dust Clumps (cm cont.)[d]	BE11/H10			58%			67%
Dust Clumps (overall)	D11	$\sigma \sim 60$ mJy	SD (33″)	40%	$\sigma \sim 100$ mK	SD (30″)	72%
RMS (North)	U11	$\sigma \sim 120$ mJy	SD (33″)	52%	$\sigma \sim 50$ mK	SD (30″)	81%
RMS YSOs (North)	U11			52%			85%
RMS H II (North)	U11			52%			78%
RMS YSO/H II (North)	U11			56%			85%
RMS (South)	U09	$\sigma \sim 250$ mJy	SD (2′)	27%	...	...	...
RMS YSOs (South)	U09			26%			
RMS H II (South)	U09			28%			
RMS YSO/H II (South)	U09			32%			
IRDC cores (overall)	Ch09	$\sigma \sim 40$ mJy	SD (33″)	35%	...	...	...
IRDC cores (quiescent)	Ch09			16%			
IRDC cores (active)	Ch09			59%			
IRDC cores (red)	Ch09			54%			
IRAS-selected HMPOs	Sr02	$\sigma \sim$400 mJy	SD (40″)	42%	...	SD (40″)	86%
IRAS-selected UC H II regions	C90	detect. limit 400 mJy	SD (40″)	67%	detect. limit. 300 mK	SD (40″)	70%
H_2O masers	A96	...	...	...	variable	SD (1.′4)	58%
OH masers	BCEP10	$\sigma \sim 40$–150 mJy	Int. ($\sim 2''$)	79%	...	...	...
Class II CH_3OH masers (6.7 GHz)	B11	$\sigma \sim 2$–10 mJy	Int. ($\sim 0.''15$)	71%	...	...	...
Class II CH_3OH masers (6.7 GHz)	Sz05	$\sigma \sim 450$ mJy	SD (40″)	52%	...	...	...
Class II CH_3OH masers (6.7 GHz)	B02	$\sigma \sim 1000$ mJy	Int. ($\sim 1''$)	62%	...	...	...
Class II CH_3OH masers (6.7 GHz)	P12	...	...	...	$\sigma \sim 30$ mK	SD (40″)	95%

Notes.
[a] A96: Anglada et al. (1996). B02: Beuther et al. (2002). BCEP10: Breen et al. (2010a). B11: Bartkiewicz et al. (2011). BE11: Breen & Ellingsen (2011). Ch09: Chambers et al. (2009). C90: Churchwell et al. (1990). D11: Dunham et al. (2011b). H10: Hill et al. (2010) P12: Pandian et al. (2012) Sr02: Sridharan et al. (2002). Sz05: Szymczak et al. (2005). U09: Urquhart et al. (2009). U11: Urquhart et al. (2011).
[b] Int. indicates interferometric observations, and estimated positional accuracy is given. SD indicates single-dish observations, and the FWHP beam size is given.
[c] See Table 2 for additional statistics on EGO subsamples. "Class I": all EGOs with a Class I maser detection in CE11, regardless of Class II association (or lack of Class II information). "Class II": all EGOs listed as Class II maser detections in CE11, regardless of Class I association. "Class I and II CH_3OH": EGOs listed as both Class I and Class II detections in CE11. "Neither CH_3OH": EGOs listed as both Class I nondetections and Class II nondetections in CE11.
[d] BE11: H_2O maser survey; H10: NH_3 survey. These surveys both target subsets of the Hill et al. (2005) dust clump sample, and divide their observed dust clumps into the same general categories. The studies are, however, independent, and BE11 do not include the NH_3 results of H10 in their analysis.

masers (95%) exceeds, to our knowledge, any reported in the literature. Our much lower detection rate toward EGOs with neither CH_3OH maser type (33%) is nonetheless higher than those toward quiescent dust clumps or IRDC cores. In general, the H_2O maser associations of EGO subsamples are similar to those of the most comparable subsamples in Table 9. For example, our detection rate for EGOs associated with Class II CH_3OH masers (regardless of Class I association) is roughly comparable to those for Class II CH_3OH maser and dust clump/Class II CH_3OH maser samples. Sensitivity is of course an important consideration, particularly in light of recent evidence that H_2O maser flux density increases as sources evolve, then turns over at a late (UC H II region) stage (Breen & Ellingsen 2011). While H_2O masers are variable, the fact that we fail to detect H_2O maser emission toward EGO G11.11−0.11, where a weak (∼0.3 Jy) H_2O maser was reported by Pillai et al. (2006a), indicates that some EGOs are associated with H_2O masers below the detection limit of our survey. Most of the surveys in Table 9 have sensitivity comparable to or better than our Nobeyama data.

The properties of the H_2O masers detected toward EGOs are typical of H_2O masers detected toward MYSOs. For example, the distributions of the velocity range of detected masers and of the velocity offset between dense gas and peak maser emission (Figures 15 and 16; see also Section 3.3.1) are generally similar to those reported in the literature, including for more evolved UC H II region samples (e.g., Churchwell et al. 1990; Anglada et al. 1996; Urquhart et al. 2011). Based on their study of

MIR-bright MYSOs and UC H II regions from the RMS sample with the Robert C. Byrd Green Bank Telescope (GBT), Urquhart et al. (2011) argue that H_2O maser properties (in particular, L_{iso}) are driven by the bolometric luminosity of the central MYSO (see also Section 4.2). The distributions of H_2O maser peak and integrated flux densities and isotropic luminosity for the MIR-bright RMS sample have high-end tails (e.g., Figure 8 of Urquhart et al. 2011); the strongest RMS H_2O masers are several orders of magnitude brighter and more luminous than the strongest H_2O masers we detect toward EGOs. However, two-sided K-S tests on these parameters indicate that the differences are not statistically significant (K-S significance 0.055, 0.249, and 0.027 for S_{peak}, S_{int}, and L_{iso}, respectively). The K-S tests are consistent with the RMS and EGO water masers being drawn from the same parent distribution.

As discussed in Sections 3.2.2 and 3.3.2, we find evidence for statistically significant differences among EGO subsamples in NH_3 but not in H_2O maser properties. Other NH_3 studies of large MYSO samples similarly find significant internal variations. The mean kinetic temperature, NH_3 line width, and NH_3 column density of BGPS sources increase with the number of associated MIR sources (albeit with considerable scatter, particularly in T_{kin}, e.g., Figure 23 of Dunham et al. 2011b). In the RMS sample, Urquhart et al. (2011) find that the mean kinetic temperature, NH_3 column density, and NH_3 line width are higher for UC H II regions than for MYSOs. Overall, the clump-scale NH_3 properties of EGOs are roughly comparable to those of other MYSO samples. Comparing Figure 4 to Figure 4 of Urquhart et al. (2011), for example, the line width, T_{kin}, and $N(NH_3)$ distributions are broadly similar (accounting for the conversion between σ_v and FWHM line width), though our sample is considerably smaller. The distribution of NH_3 column density extends to lower values for EGOs than for the RMS sample; however, this is a beam-averaged quantity, and the Nobeyama beam ($\sim$73″) is considerably larger than that of the GBT ($\sim$30″). For BGPS sources, the low end of the NH_3 column density range (based on GBT observations) extends to $\sim 1.7\times10^{13}$, more comparable to our EGO results. The EGO T_{kin} distribution (from the single-component fitting, for consistency with other studies) lacks the high temperature (>40 K) tail seen in RMS, UC H II region, and even BGPS samples (Urquhart et al. 2011; Dunham et al. 2011b; Churchwell et al. 1990). The mean T_{kin} for the EGO sample (23.6 K) is higher than that of the Dunham et al. (2011b) sample (17.4 K, for their "T_K subsample" consisting of (2,2) detections) and similar to that of the RMS sample as a whole ($\sim$22 K).

These general comparisons illustrate that the H_2O maser and clump-scale NH_3 properties of EGOs are consistent with their being a population of young MYSOs. However, we emphasize that the differences within samples (EGOs, RMS sources, BGPS sources) are often as great or greater than the differences between them. These *intra*-sample differences emphasize the importance of studying multiple star formation tracers across wavelength regimes.

4.1.2. Comparison with Star Formation Criteria

By combining our Nobeyama NH_3 data with the BGPS, we can also consider the dust clumps associated with EGOs in the context of proposed star formation thresholds. Unlike purely mm-selected samples (e.g., Dunham et al. 2011b), all of the clumps we consider are associated with EGOs, and thus demonstrably star forming (many are also associated with other MIR sources). Figure 20 shows a mass–radius plot for clumps with well-determined (non-limit) T_{kin} and radii, with the clump masses estimated assuming $T_{dust} = T_{kin}$ from the single-component NH_3 fits. The errors bars shown in Figure 20 indicate the range in radius associated with the distance uncertainty from Table 8, and the range in mass associated with the combined uncertainties in the BGPS integrated flux density, the BGPS flux correction factor, and the distance (see also Section 3.4). The error bars do not include systematic uncertainty in the radius estimate due to different geometries (see also Rosolowsky et al. 2010). Three proposed star formation thresholds are indicated in Figure 20: (1) the Krumholz & McKee (2008) threshold for massive star formation of 1 g cm^{-2} (4788 $M_\odot$ pc^{-2}), (2) the average of the Lada et al. (2010) and Heiderman et al. (2010) thresholds for "efficient" star formation (122.5 $M_\odot$ pc^{-2}), and (3) the Kauffmann & Pillai (2010) and Kauffmann et al. (2010) threshold for massive star formation. We refer to these as the KM, HL, and KP thresholds, respectively. As in the recent BGPS study of Dunham et al. (2011b), we scale the KP criterion of $M(r) > 870\,M_\odot\ (r/\mathrm{pc})^{1.33}$ to $M(r) > 580\,M_\odot\ (r/\mathrm{pc})^{1.33}$ to account for the difference between our assumed dust opacity and that adopted by Kauffmann & Pillai (2010). Adopting the nominal clump mass and radius values from Table 8, 70% (35/50) of the sources shown in Figure 20 exceed the KP threshold, and 76% (38/50) exceed the HL threshold; as in the Dunham et al. (2011b) study of BGPS sources, none of our EGO clumps meet the KM criterion. We emphasize that the points in Figure 20 represent *average* surface densities over entire BGPS sources, and that the BGPS and Nobeyama observations probe large scales. At a typical distance of 4 kpc, the 33″ BGPS beam is $\sim$0.64 pc, and the 73″ Nobeyama beam $\sim$1.4 pc. Interferometric

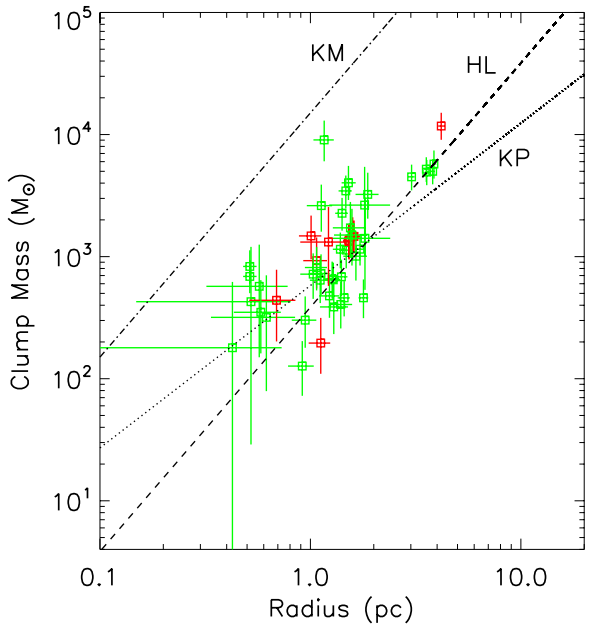

Figure 20. Clump mass vs. radius for BGPS sources associated with EGOs. Clump masses are calculated assuming $T_{dust} = T_{kin}$ from single-component NH_3 fitting. Open squares indicate nominal values from Table 8. The error bars indicate the range in radius associated with the uncertainty in distance (Table 8) and the range in mass associated with the combined uncertainties in the BGPS integrated flux density, the BGPS flux correction factor, and the distance. The star formation thresholds of Krumholz & McKee (2008), Heiderman et al. (2010) and Lada et al. (2010), and Kauffmann & Pillai (2010) are indicated as dot-dashed, dashed, and dotted lines, respectively. Only sources for which the T_{kin} and radius are well-determined (non-limit) are plotted. H_2O maser detections are plotted in green, and H_2O maser nondetections in red.

(A color version of this figure is available in the online journal.)

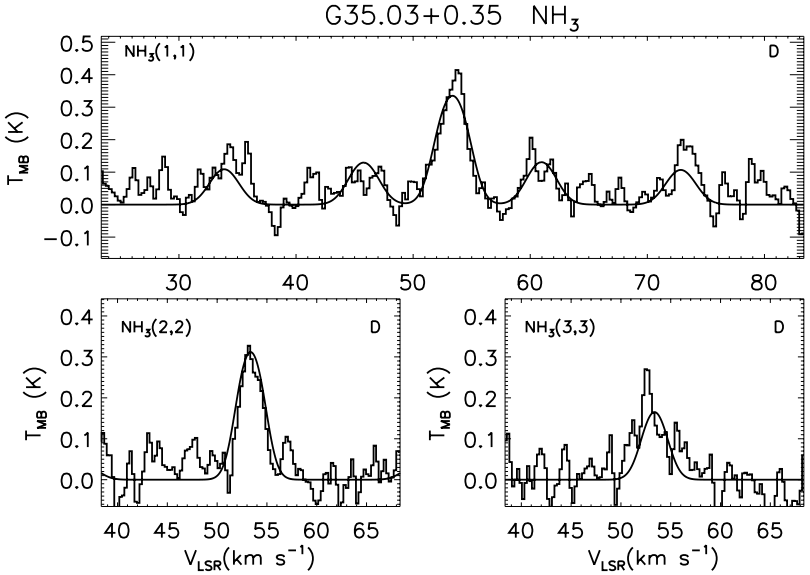

Figure 21. Nobeyama NH_3 spectra of the EGO G35.03+0.35, in which Brogan et al. (2011) detect an $NH_3(3,3)$ maser with the VLA.

observations of EGOs, and of other MYSOs, provide ample evidence for substructure (e.g., cores and (proto)clusters) and variations in gas temperature on much smaller scales (e.g., Cyganowski et al. 2011a; Brogan et al. 2011).

Having placed clumps on the mass–radius plot using (primarily) the BGPS data, we use our Nobeyama survey data to look for differences in the properties of clumps above/below the HL and KP thresholds. As in our comparison of EGO subsamples (Section 3.2.2), we ran two-sided K-S tests on eight NH_3 parameters (the NH_3 (1,1), (2,2), and (3,3) peaks (T_{MB}), σ_v, $\tau_{(1,1)}$, η_{ff}, $N(NH_3)$, and T_{kin}). We find statistically significant differences only for the $NH_3(1,1)$ and (2,2) peak temperatures and the filling fraction η_{ff},[17] with clumps below the HL and KP thresholds having lower values of these parameters. The K-S tests indicate no statistically significant differences in the distributions of the physical properties σ_v, T_{kin}, and $N(NH_3)$ for clumps above/below the thresholds. Interestingly, and perhaps counterintuitively, the H_2O maser detection rates are *higher* for EGOs associated with clumps *below* the HL and KP thresholds (Figure 20). The H_2O maser detection rate is 0.74(±0.07) for sources that meet the KP criterion, and 0.93(±0.06) for sources that do not (uncertainties in detection rates calculated using binomial statistics). Similarly, the H_2O maser detection rates are 0.76(±0.07) and 0.92(±0.08) for sources that do/do not meet the HL criterion, respectively.

The nature of the EGOs associated with clumps that fall below the KP threshold requires further investigation. The higher H_2O maser detection rate toward clumps below the KP threshold is surprising, and the lack of difference in NH_3 properties suggests a continuum, rather than a sharp distinction. Additionally, one source that falls below the KP threshold, G24.94+0.07, is associated with 6.7 GHz Class II CH_3OH maser and cm continuum emission (C09, C11b), both indicative of the presence of an MYSO. We note that the placement of clumps on a mass–radius plot is sensitive to assumptions about clump temperature structure (or lack thereof). For EGOs in our study fit with warm and cool components, the warm component constitutes a small fraction of the clump mass; the bulk of the material generally has temperature $T_{cool} < T_{single\ comp.}$, and so the isothermal assumption usually underestimates the clump mass (Section 3.4, Table 8). Interferometric NH_3 observations show significant temperature structure on scales within the Nobeyama beam for G35.03+0.35 (Figure 3 of Brogan et al. 2011), a source that did *not* require two temperature components to fit its Nobeyama NH_3 spectra (Figure 21). On larger scales, many of the BGPS sources associated with EGOs (and plotted in Figure 20) extend beyond the Nobeyama beam. If isothermal clump masses for EGOs tended to be underestimates—due to temperature structure on small or large scales—this would move points up in Figure 20, and increase the proportion of sources above the KP threshold. Additional data—such as NH_3 maps with sufficient resolution to probe the temperature structure of the BGPS clumps—are needed to address this issue. Interferometric (sub)mm observations, to resolve the dust continuum emission and detect individual cores, and improved constraints on bolometric luminosity (e.g., from HiGal) will also help to clarify the nature of the driving sources.

4.2. Correlations between H_2O Maser and Clump Properties?

Over the past decades, numerous authors have investigated possible correlations amongst clump, H_2O maser, and driving source properties in MYSO samples (e.g., Churchwell et al. 1990; Anglada et al. 1996; Breen & Ellingsen 2011; Urquhart et al. 2011). Recently, two studies have reported correlations between H_2O maser luminosity and the properties of the driving source or surrounding clump. For their sample of ∼300 RMS sources with H_2O maser detections, Urquhart et al. (2011) find that H_2O maser luminosity is positively correlated with bolometric luminosity for both MYSOs and H II regions. In contrast, Breen & Ellingsen (2011) report an anticorrelation between clump H_2 number density and H_2O maser luminosity, which they attribute to an evolutionary effect: more evolved sources have more luminous water masers and are associated with lower-density clumps. All of these studies have combined H_2O maser and *either* NH_3 or (sub)mm dust continuum data. Breen & Ellingsen (2011), in particular, caution that the clump densities used in their study (from Hill et al. 2005) were calculated assuming a single temperature for all clumps, and that temperature differences could create the apparent density

[17] We note η_{ff} is mildly degenerate with $T_{MB}(1,1)$.

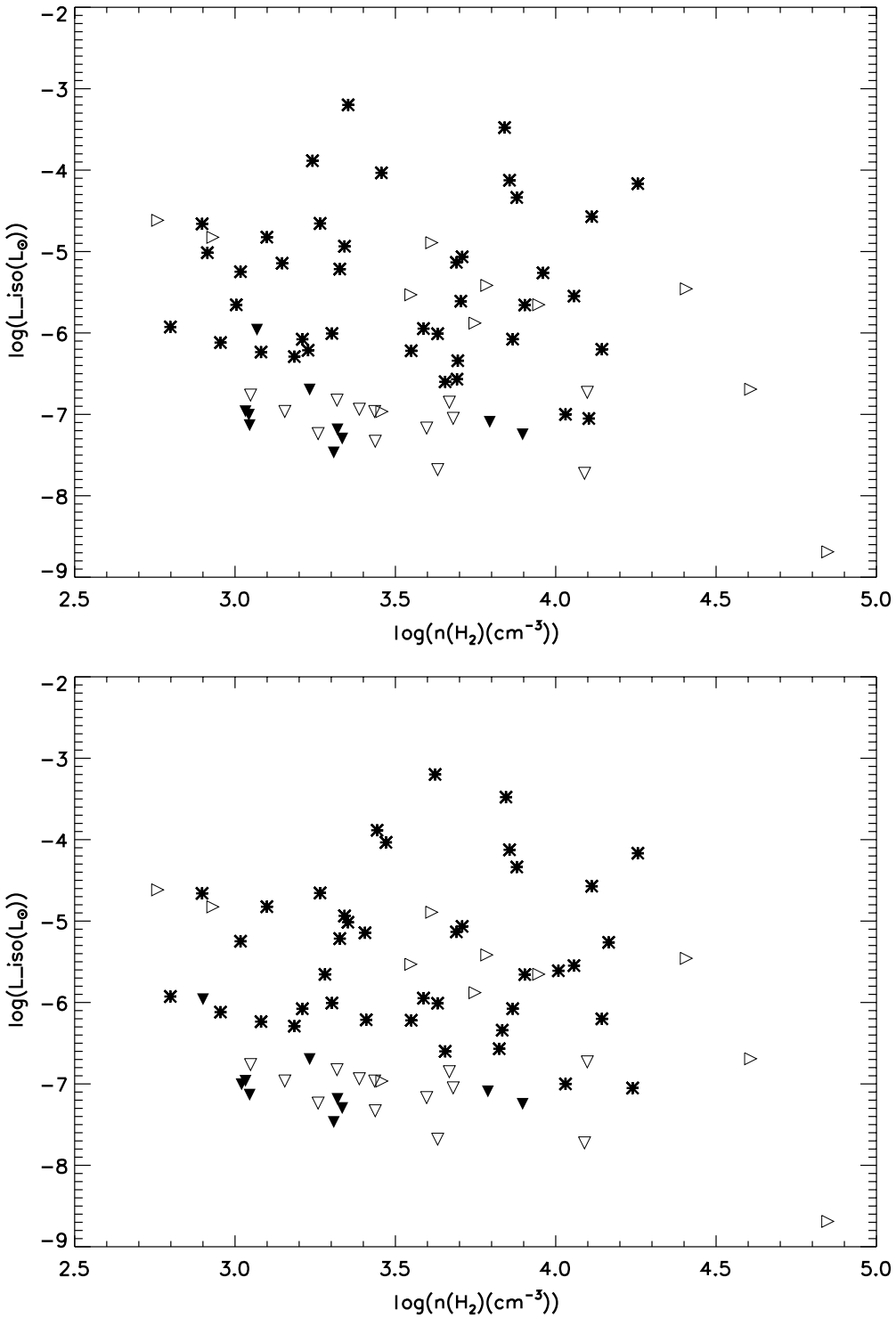

Figure 22. Top: isotropic H_2O maser luminosity vs. volume-averaged number density estimated using T_{kin} from single-component NH_3 fitting. "*" indicates EGOs with H_2O maser detections in our survey and well-determined density estimates (e.g., neither T_{kin} nor R is a limit). Filled downward-pointing triangles indicate 4σ $L(H_2O)$ upper limits for EGOs with well-determined density estimates that are H_2O maser nondetections in our survey. EGOs for which the estimated density is a lower limit are represented as open triangles: open right-facing triangles indicate H_2O maser detections, and open downward-pointing triangles 4σ $L(H_2O)$ upper limits for H_2O maser nondetections. Bottom: same as top, except the density estimates account for warm and cool components when the NH_3 spectra are fit with two components (see Section 3.4).

trend. Our NH_3 and H_2O maser survey, in combination with the BGPS, provides the necessary data to fully explore correlations between maser and clump properties, and test evolutionary interpretations.

Figure 22 shows that when clump densities are calculated for our sample using measured clump temperatures, there is no correlation between H_2O maser luminosity and clump density: the log–log plot of $L(H_2O)$ versus number density is a scatter plot. This remains the case even when accounting for the contributions of warm and cool gas for sources that require two-component NH_3 fits. The partial correlation coefficients, computed with the distance squared as an independent

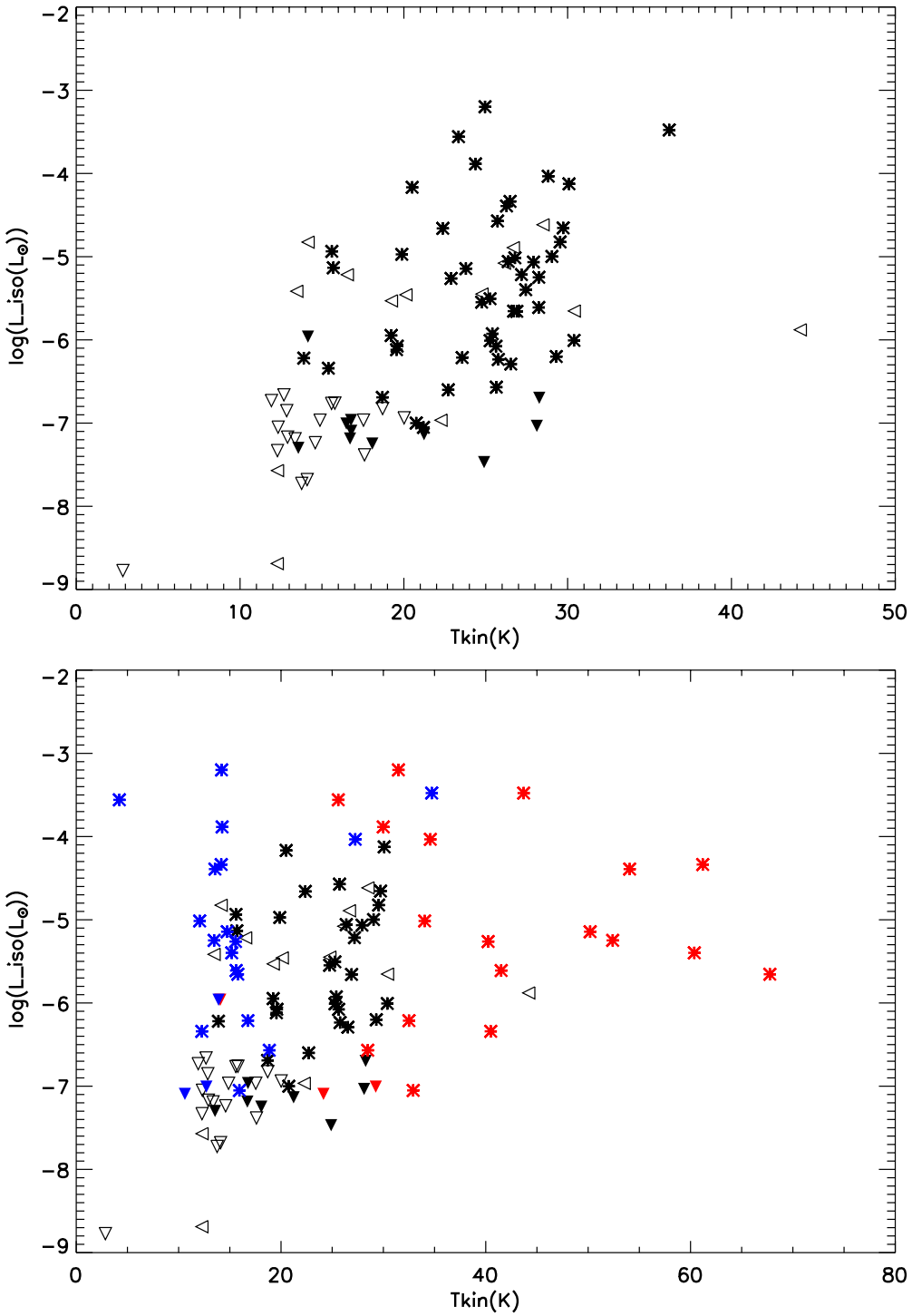

Figure 23. Top: isotropic H_2O maser luminosity vs. T_{kin} from single-component NH_3 fitting. "*" indicates EGOs with H_2O maser and $NH_3(2,2)$ detections in our survey (e.g., T_{kin} well determined). Filled downward-pointing triangles indicate 4σ $L(H_2O)$ upper limits for EGOs undetected in H_2O maser emission but detected in $NH_3(2,2)$. EGOs undetected in $NH_3(2,2)$—for which the best-fit T_{kin} is treated as an upper limit—are represented as open triangles: open left-facing triangles indicate H_2O maser detections, and open downward-pointing triangles 4σ $L(H_2O)$ upper limits for H_2O maser nondetections. Bottom: same as top, except for sources fit with two NH_3 components, T_{kin}(cool) is plotted in blue and T_{kin}(warm) in red.

(A color version of this figure is available in the online journal.)

parameter, are 0.04 and 0.06 for the one- and two-temperature component density estimates, respectively (only sources with H_2O maser detections and non-limit densities are included in the calculation). These low values confirm that H_2O maser luminosity and clump number density are uncorrelated in our data.

In contrast, H_2O maser luminosity is weakly correlated with clump temperature, as shown in Figure 23. For EGOs detected in both H_2O maser and $NH_3(2,2)$ emission, the partial correlation coefficient is 0.36 for T_{kin} derived from the single-component fits (again computed with the distance squared as an independent parameter). Interestingly, if we recompute the partial correlation

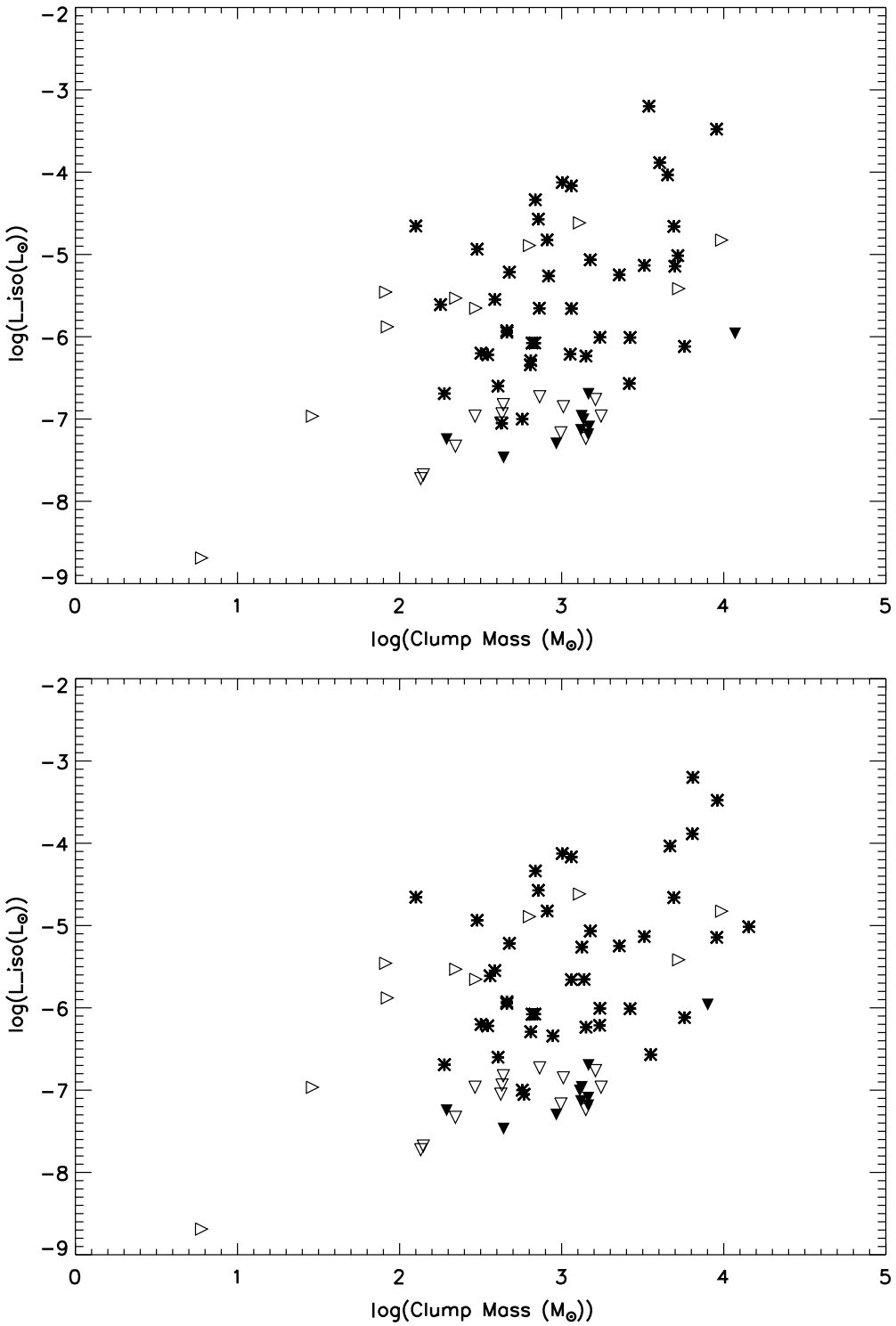

Figure 24. Top: isotropic H_2O maser luminosity vs. clump mass, assuming $T_{dust} = T_{kin}$ from single-component NH_3 fitting. "*" indicates EGOs with H_2O maser and NH_3(2,2) detections in our survey (e.g., T_{kin} well determined). Filled downward-pointing triangles indicate 4σ $L(H_2O)$ upper limits for EGOs undetected in H_2O maser emission but detected in NH_3(2,2). EGOs undetected in NH_3(2,2)—for which the best-fit T_{kin} is an upper limit and the clump mass thus a lower limit (Section 3.4)—are represented as open triangles: open right-facing triangles indicate H_2O maser detections, and open downward-pointing triangles 4σ $L(H_2O)$ upper limits for H_2O maser nondetections. Bottom: same as top, except the mass estimate accounts for warm and cool components for sources fit with two NH_3 components (Section 3.4).

coefficient using the T_{kin} of the warm component for sources that require two-component fits (and the single-component T_{kin} for all other sources), the value is reduced to 0.22. This is somewhat surprising, since the warm component traces gas nearer to, and heated by, the central MYSO.

We also find a weak positive correlation between H_2O maser luminosity and clump mass (Figure 24). Calculating clump masses assuming $T_{dust} = T_{kin}$ from the single-component NH_3 fits, the partial correlation coefficient is 0.44 (for EGOs detected in both H_2O maser and NH_3(2,2) emission, so that T_{kin}

is well determined). The calculated partial correlation coefficient is very similar (0.43) if the presence of two temperature components is accounted for when estimating the clump mass (Section 3.4). A K-S test indicates no statistically significant difference between the mass distributions of clumps with/without H_2O masers, in contrast to earlier studies (Chambers et al. 2009; Breen & Ellingsen 2011). The significance of the K-S statistic is 0.26 using the isothermal clump masses (for EGOs with (2,2) detections and so well-determined T_{kin}, as above), and increases to 0.45 if clump masses are estimated accounting for the two temperature components. Both previous studies assumed dust temperatures, and Chambers et al. (2009) found that the probability that their cores with/without H_2O masers were drawn from the same distribution increased dramatically (by a factor of >50, to 0.11) if they assumed a higher temperature for active cores (compared to assuming a single temperature for all cores). The θ_{FWHM} of the BGPS data ($\sim$33″) is larger than that of the SIMBA data used by Breen & Ellingsen (2011) ($\sim$24″; Hill et al. 2005) or the IRAM 30 m data used by Chambers et al. (2009) ($\sim$11″; Rathborne et al. 2006). Additional data (such as temperature measurements for the Chambers et al. 2009 and Breen & Ellingsen 2011 sources) would be required to assess whether this difference in scale contributes to the difference in findings.

Our results are consistent with the positive correlation between H_2O maser and bolometric luminosity reported by Urquhart et al. (2011) for RMS sources. In this picture, the key factor is the bolometric luminosity of the driving MYSO, with more luminous MYSOs exciting more luminous H_2O masers. The observed correlations of H_2O maser and clump properties (temperature and mass) are then understood in terms of the relationship between a clump and the massive star(s) it forms. The final mass of an actively accreting MYSO is limited by the available mass reservoir, and studies of more evolved sources (UC H II regions) indicate that higher-mass clumps form higher-mass (and thus more luminous) stars (e.g., Johnston et al. 2009). The more luminous an MYSO, the more energy it will impart to its environs, and the more it will heat the gas and dust of the surrounding clump.

4.3. NH_3(3,3) Masers

While NH_3(3,3) maser emission in an MSFR was first reported several decades ago (DR21(OH); Mangum & Wootten 1994), the number of known examples—all detected with the VLA—has remained small (e.g., W51, NGC 6334I, IRAS 20126+4106, G5.89−0.39: Zhang & Ho 1995; Kraemer & Jackson 1995; Zhang et al. 1999; Hunter et al. 2008). Two recent, large-scale single-dish surveys each report a single NH_3(3,3) maser candidate: a blind survey of 100 deg^2 of the Galactic plane (HOPS; Walsh et al. 2011), and a targeted survey of $\sim$600 RMS sources (Urquhart et al. 2011). This paucity of candidates led Urquhart et al. (2011) to suggest that bright NH_3(3,3) masers are rare.

One of our targets, G35.03+0.35, was recently observed in NH_3(1,1)-(6,6) with the VLA (Brogan et al. 2011). In addition to complex thermal NH_3 emission from a (proto)cluster, nonthermal NH_3(3,3) and (6,6) emission are clearly detected (Brogan et al. 2011, Figure 2; peak (3,3) intensity $<$70 mJy beam^{-1}). Figure 21 shows our Nobeyama NH_3 spectra of G35.03+0.35: while there is a narrow NH_3(3,3) emission feature that is not well fit by the model, the signal-to-noise ratio is insufficient to identify it as a candidate maser from the single-dish data. This comparison demonstrates that single-dish surveys readily miss weak NH_3(3,3) masers detected with interferometers; sensitive interferometric observations are required to assess the prevalence of NH_3 masers in MSFRs, and their association with other maser types (see also Brogan et al. 2011, 2012).

4.4. Future Work

Our analysis of our Nobeyama EGO survey shows that the presence of NH_3(2,2) and (3,3) emission, H_2O masers, and Class I and II CH_3OH masers are strongly correlated. These star formation indicators tend to occur in concert (at least on the scales probed by single-dish surveys), and identify a (sub)population of EGOs in which central MYSO(s) are substantially affecting their environments, heating the surrounding gas and exciting maser emission. Notably, maser emission and warm dense gas appear to pinpoint such sources more effectively than MIR indicators such as the "likely"/"possible" classification of C08 or the presence/absence of IRDCs. These sources are excellent targets for high-resolution follow-up observations aimed at understanding the importance of different (proto)stellar feedback mechanisms in MSFRs, as demonstrated by the SMA, CARMA, and VLA studies of Cyganowski et al. (2011a, 2011b) and Brogan et al. (2011). These EGOs are also important testbeds for proposed maser evolutionary sequences, as discussed in more detail below.

Less clear is the nature of those EGOs detected only in NH_3(1,1) emission in our survey. An examination of their GLIMPSE images suggests they are a heterogeneous group, including both EGOs in IRDCs (e.g., G12.02−0.21) and EGOs adjacent to 8 and 24 μm bright nebulae (e.g., G29.91−0.81). Some examples of each of these MIR source types are detected in H_2O maser emission, while others are not. The MIR morphologies of EGOs without detected H_2O masers in our survey are similarly heterogeneous, and some H_2O maser nondetections are associated with NH_3(2,2) and (3,3) emission. Higher-resolution observations are required to localize the NH_3 and H_2O maser emission detected in our Nobeyama data with respect to the MIR emission

We emphasize that high-resolution observations are crucial for building an evolutionary sequence for MYSOs, and placing EGOs within it. In general, multiple MIR sources are present within the Nobeyama beam, and detailed studies of EGOs to date reveal mm and cm-λ multiplicity on $\sim$0.1 pc scales. Furthermore, the members of (proto)clusters associated with EGOs exhibit a range of star formation indicators, suggestive of a range of evolutionary states (e.g., Cyganowski et al. 2011a; Brogan et al. 2011).

EGOs are notably rich in maser emission, and maser studies have and continue to provide key insights into the nature of EGOs; their copious maser emission likewise provides opportunities to use EGOs to advance our understanding of masers in MSFRs. H_2O, Class I and II CH_3OH, and OH masers are ubiquitous in regions of massive star formation, and much effort has been devoted to placing these different maser types into an evolutionary sequence. Of particular interest is which maser type appears first—and thus pinpoints the earliest stages of massive star formation. In most proposed sequences, Class I CH_3OH masers are identified with the earliest stages of MYSO evolution, with the youngest sources being those associated only with Class I CH_3OH masers (e.g., Ellingsen 2006; Ellingsen et al. 2007; Breen et al. 2010b). However, recent work suggests that Class I CH_3OH masers may be excited by shocks driven by expanding H II regions as well as by outflows (e.g., Voronkov

et al. 2010), such that Class I CH_3OH masers may outlast the Class II maser stage and/or arise more than once during MYSO evolution (e.g., Chen et al. 2011; Voronkov et al. 2012). Breen & Ellingsen (2011) and Caswell & Breen (2010) have also recently proposed that H_2O masers—particularly those with blueshifted high-velocity features—may be the earliest signposts of MYSO formation, preceding the Class II CH_3OH maser stage.

Statistical comparisons of "Class I only" and "Class II only" EGOs based on our data are limited by the small sample sizes. It is notable, however, that the NH_3(2,2) and H_2O maser detection rates toward these subsamples are comparable, particularly considering the small number statistics. Likewise, Figures 12 and 18 show no clear patterns in their NH_3 or H_2O maser properties that would suggest a trend in evolutionary state. The parameter space occupied by Class I-only and Class II-only sources in these plots also largely overlaps with that occupied by EGOs associated with both CH_3OH maser types. Though the comparison is again limited by small-number statistics, the difference in the NH_3(3,3) detection rates (63%/14% for Class I/II-only sources) is intriguing, particularly given the association of Class I CH_3OH and NH_3(3,3) masers (e.g., Brogan et al. 2011).

Progress in our understanding of masers as evolutionary indicators for MSF requires identifying candidate youngest sources, and studying them in detail (see also Cyganowski et al. 2012). The (small) samples of EGOs with H_2O+Class I CH_3OH and H_2O+Class II CH_3OH masers identified in our survey will be promising targets for such studies, as will the samples of H_2O-only, Class I CH_3OH-only, and Class II CH_3OH-only sources. Sensitive, high-resolution maser observations are needed: (1) to localize the maser emission, and determine whether or not all maser species are associated with the same MYSO and (2) to search for weak masers and establish whether maser types undetected in single-dish surveys are truly absent. The expanded capabilities of the Karl G. Jansky VLA are well suited to such studies. High-resolution cm-(sub)mm wavelength line and continuum observations will also constrain the properties of compact cores and outflows, allowing maser activity to be correlated with other signposts of star formation at the scale of individual active sources.

5. CONCLUSIONS

We have surveyed all 94 GLIMPSE EGOs visible from the northern hemisphere ($\delta \gtrsim -20^\circ$) in H_2O maser and NH_3(1,1), (2,2), and (3,3) emission with the Nobeyama 45 m telescope. Our results provide strong evidence that EGOs, as a population, are associated with dense gas and active star formation, and also reveal statistically significant variation amongst EGO subsamples:

1. H_2O masers, which are associated with outflows and require high densities ($n(H_2) \sim 10^8$–10^{10} cm^{-3}), are detected toward ~68% of EGOs surveyed.
2. The NH_3(1,1) detection rate is ~97%, confirming that EGOs are associated with dense molecular gas.
3. Two-component models provide a significantly improved fit for ~23% of our NH_3 spectra, indicating contributions from both warm inner regions and cooler envelopes along the line of sight.
4. H_2O maser emission is strongly correlated with the presence of warm, dense gas, as indicated by emission in the higher-excitation NH_3 transitions. The H_2O maser detection rate is 81% toward EGOs detected in NH_3(2,2) and (3,3) emission, and only 44% toward EGOs detected only in NH_3(1,1). We find statistically significant differences in the distributions of NH_3 column density, kinetic temperature, and NH_3 line width for EGOs with/without H_2O maser detections: EGOs with H_2O masers have higher median $N(NH_3)$, T_{kin}, and σ_v.
5. H_2O maser and NH_3(2,2) and (3,3) detection rates are higher toward EGOs classified as "likely" outflow candidates based on their MIR morphology than toward EGOs classified as "possible" outflow candidates. However, statistical tests show significant differences only in the distributions of NH_3(1,1) and (2,2) peak temperatures (T_{MB}), not in physical properties.
6. EGOs associated with IRDCs have higher NH_3(2,2) and (3,3) detection rates than EGOs not associated with IRDCs. We find statistically significant differences in the distributions of NH_3(1,1) peak (T_{MB}), NH_3 line width, and NH_3 beam filling fraction: EGOs associated with IRDCs have higher median NH_3(1,1) T_{MB}, and lower median σ_v, than EGOs not associated with IRDCs.
7. The H_2O maser, NH_3(2,2), and NH_3(3,3) detection rates toward EGOs with both Class I and II CH_3OH masers are the highest of any EGO subsample we consider: 95%, 90% and 81%, respectively. In contrast, we detect H_2O masers and the higher-excitation NH_3 lines toward only 33% (H_2O), 20% (2,2) and 7% (3,3) of EGOs with neither type of CH_3OH maser. We find statistically significant differences in the distributions of NH_3(1,1) peak temperature (T_{MB}), NH_3 column density, and NH_3 line width for EGOs associated with both types/neither type of CH_3OH masers: EGOs associated with both Class I and II CH_3OH masers have higher median NH_3(1,1) T_{MB}, $N(NH_3)$, σ_v, and T_{kin}.
8. While H_2O maser detection rates vary across EGO subsamples, we find no evidence for statistically significant differences in the properties of detected H_2O masers.

Our H_2O maser and NH_3 survey, in combination with the 1.1 mm continuum BGPS, provides the necessary data to explore connections between H_2O maser and clump properties: H_2O maser spectra, clump-scale T_{kin} measurements from NH_3, and clump masses and densities from the 1.1 mm dust continuum emission and T_{kin} measurements. These combined data show no correlation between isotropic H_2O maser luminosity and volume-averaged clump density. H_2O maser luminosity is weakly positively correlated with clump temperature and with clump mass, consistent with reported correlations between H_2O maser luminosity and the bolometric luminosity of the driving source.

We interpret the observed correlations of H_2O maser and clump properties in terms of the relationship between a clump and the massive star(s) it forms. For more evolved sources (UC H II regions), studies indicate that higher-mass clumps form higher-mass (and thus more luminous) stars (e.g., Johnston et al. 2009). For an actively accreting MYSO, the available mass reservoir sets the limit on its final, stellar mass. The more luminous (and massive) an MYSO, the more energy it will impart to its environs, and the more it will heat the gas and dust of the surrounding clump.

We find that NH_3(2,2) and (3,3) emission, H_2O masers, and Class I and II CH_3OH masers are strongly correlated, at least on the scales probed by single-dish surveys. These star formation indicators pinpoint EGOs in which the central MYSO(s) are substantially affecting their environments, more effectively than

MIR indicators (such as the "likely"/"possible" classification of C08 or the presence/absence of IRDCs). We also identify small samples of EGOs associated with only one maser type; the H_2O-only and Class I CH_3OH-only sources are candidates for extremely young MYSOs. Constructing an evolutionary scheme for MYSOs requires localizing maser and dense gas emission at the scale of individual (proto)stars. The expanded capabilities of the Karl G. Jansky VLA will enable such studies for statistically meaningful samples.

We thank the staff at the Nobeyama Radio Observatory for their support during our observing runs. This research has made use of NASA's Astrophysics Data System Bibliographic Services and the SIMBAD database operated at CDS, Strasbourg, France. Support for this work was provided by NSF grant AST-0808119. C.J.C. was partially supported during this work by a National Science Foundation Graduate Research Fellowship, and is currently supported by an NSF Astronomy and Astrophysics Postdoctoral Fellowship under award AST-1003134. C.J.C. thanks M. Reid for helpful discussions about kinematic distances, and J. Brown, L. Chomiuk, and H. Kirk for IDL insight. E.R. is supported by a Discovery Grant from NSERC of Canada.

REFERENCES

Aguirre, J. E., Ginsburg, A. G., Dunham, M. K., et al. 2011, ApJS, 192, 4
Anglada, G., Estalella, R., Pastor, J., Rodriguez, L. F., & Haschick, A. D. 1996, ApJ, 463, 205
Araya, E., Hofner, P., Sewiło, M., et al. 2007, ApJ, 669, 1050
Bae, J.-H., Kim, K.-T., Youn, S.-Y., et al. 2011, ApJS, 196, 21
Bartkiewicz, A., Szymczak, M., Pihlström, Y. M., et al. 2011, A&A, 525, A120
Beuther, H., Walsh, A., Schilke, P., et al. 2002, A&A, 390, 289
Bourke, T. L., Hyland, A. R., & Robinson, G. 2005, ApJ, 625, 883
Breen, S. L., Caswell, J. L., Ellingsen, S. P., & Phillips, C. J. 2010a, MNRAS, 406, 1487
Breen, S. L., & Ellingsen, S. P. 2011, MNRAS, 416, 178
Breen, S. L., Ellingsen, S. P., Caswell, J. L., & Lewis, B. E. 2010b, MNRAS, 401, 2219
Breen, S. L., Ellingsen, S. P., Caswell, J. L., et al. 2011, ApJ, 733, 80
Brogan, C. L., Hunter, T. R., Cyganowski, C. J., et al. 2011, ApJL, 739, L16
Brogan, C. L., Hunter, T. R., Cyganowski, C. J., et al. 2012, in IAU Symp. 287, Cosmic Masers - from OH to H_0, ed. R. S. Booth, E. M. L. Humphreys, & V. H. T. Vlemmings (Cambridge: Cambridge Univ. Press), 497
Brunthaler, A., Reid, M. J., Menten, K. M., et al. 2009, ApJ, 693, 424
Caswell, J. L., & Breen, S. L. 2010, MNRAS, 407, 2599
Caswell, J. L., & Green, J. A. 2011, MNRAS, 411, 2059
Chambers, E. T., Jackson, J. M., Rathborne, J. M., & Simon, R. 2009, ApJS, 181, 360
Chen, X., Ellingsen, S. P., Shen, Z.-Q., Titmarsh, A., & Gan, C.-G. 2011, ApJS, 196, 9
Chen, X., Shen, Z.-Q., Li, J.-J., Xu, Y., & He, J.-H. 2010, ApJ, 710, 150
Churchwell, E., Babler, B. L., Meade, M. R., et al. 2009, PASP, 121, 213
Churchwell, E., Walmsley, C. M., & Cesaroni, R. 1990, A&AS, 83, 119
Cragg, D. M., Sobolev, A. M., & Godfrey, P. D. 2005, MNRAS, 360, 533
Cyganowski, C. J., Brogan, C. L., & Hunter, T. R. 2007, AJ, 134, 346
Cyganowski, C. J., Brogan, C. L., Hunter, T. R., & Churchwell, E. 2009, ApJ, 702, 1615
Cyganowski, C. J., Brogan, C. L., Hunter, T. R., Churchwell, E., & Zhang, Q. 2011a, ApJ, 729, 124
Cyganowski, C. J., Brogan, C. L., Hunter, T. R., & Churchwell, E. 2011b, ApJ, 743, 56
Cyganowski, C. J., Brogan, C. L., Hunter, T. R., et al. 2012, ApJL, 760, L20
Cyganowski, C. J., Whitney, B. A., Holden, E., et al. 2008, AJ, 136, 2391
Davis, C. J., Kumar, M. S. N., Sandell, G., et al. 2007, MNRAS, 374, 29
De Buizer, J. M., & Vacca, W. D. 2010, AJ, 140, 196
Devine, K. E., Chandler, C. J., Brogan, C., et al. 2011, ApJ, 733, 44
Dunham, M. K., Robitaille, T. P., Evans, N. J., II, et al. 2011a, ApJ, 731, 90
Dunham, M. K., Rosolowsky, E., Evans, N. J., II, Cyganowski, C., & Urquhart, J. S. 2011b, ApJ, 741, 110
Dunham, M. K., Rosolowsky, E., Evans, N. J., II, et al. 2010, ApJ, 717, 1157
Elitzur, M., Hollenbach, D. J., & McKee, C. F. 1989, ApJ, 346, 983
Ellingsen, S. P. 2006, ApJ, 638, 241
Ellingsen, S. P., Breen, S. L., Sobolev, A. M., et al. 2011, ApJ, 742, 109
Ellingsen, S. P., Voronkov, M. A., Cragg, D. M., et al. 2007, in IAU Symp. 242, Astrophysical Masers and their Environments, ed. J. M. Chapman & W. A. Baan (Cambridge: Cambridge Univ. Press), 213
Evans, N. J., II 1999, ARA&A, 37, 311
Fazio, G. G., Hora, J. L., Allen, L. E., et al. 2004, ApJS, 154, 10
Forster, J. R., & Caswell, J. L. 1999, A&AS, 137, 43
Green, J. A., & McClure-Griffiths, N. M. 2011, MNRAS, 417, 2500
Green, J. A., McClure-Griffiths, N. M., Caswell, J. L., et al. 2009, ApJL, 696, L156
He, J. H., Takahashi, S., & Chen, X. 2012, ApJS, 202, 1
Heiderman, A., Evans, N. J., II, Allen, L. E., Huard, T., & Heyer, M. 2010, ApJ, 723, 1019
Hill, T., Burton, M. G., Minier, V., et al. 2005, MNRAS, 363, 405
Hill, T., Longmore, S. N., Pinte, C., et al. 2010, MNRAS, 402, 2682
Hoare, M. G., Lumsden, S. L., Oudmaijer, R. D., et al. 2005, in IAU Symp. 227, Massive Star Birth: A Crossroads of Astrophysics, ed. R. Cesaroni, E. Churchwell, M. Felli, & C. M. Walmsley (Cambridge: Cambridge Univ. Press), 370
Hofner, P., & Churchwell, E. 1996, A&AS, 120, 283
Hunter, T. R., Brogan, C. L., Indebetouw, R., & Cyganowski, C. J. 2008, ApJ, 680, 1271
Hunter, T. R., Brogan, C. L., Megeath, S. T., et al. 2006, ApJ, 649, 888
Ikeda, M., Nishiyama, K., Ohishi, M., & Tatematsu, K. 2001, in ASP Conf. Proc. 238, Astronomical Data Analysis Software and Systems X, ed. F. R. Harnden, Jr., F. A. Primini, & H. E. Payne (San Francisco, CA: ASP), 522
Johnston, K. G., Shepherd, D. S., Aguirre, J. E., et al. 2009, ApJ, 707, 283
Kauffmann, J., & Pillai, T. 2010, ApJL, 723, L7
Kauffmann, J., Pillai, T., Shetty, R., Myers, P. C., & Goodman, A. A. 2010, ApJ, 716, 433
Kraemer, K. E., & Jackson, J. M. 1995, ApJL, 439, L9
Krumholz, M. R., & McKee, C. F. 2008, Natur, 451, 1082
Kurayama, T., Nakagawa, A., Sawada-Satoh, S., et al. 2011, PASJ, 63, 513
Kurtz, S., Hofner, P., & Álvarez, C. V. 2004, ApJS, 155, 149
Lada, C. J., Lombardi, M., & Alves, J. F. 2010, ApJ, 724, 687
Leurini, S. 2004, PhD thesis, Max Planck Inst. fur Radioastronomie
Mangum, J. G., & Wootten, A. 1994, ApJL, 428, L33
Markwardt, C. B. 2009, in ASP Conf. Ser. 411, Astronomical Data Analysis Software and Systems XVIII, ed. D. A. Bohlender, D. Durand, & P. Dowler (San Francisco, CA: ASP), 251
Minier, V., Ellingsen, S. P., Norris, R. P., & Booth, R. S. 2003, A&A, 403, 1095
Mueller, K. E., Shirley, Y. L., Evans, N. J., II, & Jacobson, H. R. 2002, ApJS, 143, 469
Pandian, J. D., Leurini, S., Menten, K. M., Belloche, A., & Goldsmith, P. F. 2008, A&A, 489, 1175
Pandian, J. D., Wyrowski, F., & Menten, K. M. 2012, ApJ, 753, 50
Pillai, T., Wyrowski, F., Menten, K. M., & Krügel, E. 2006a, A&A, 447, 929
Pillai, T., Wyrowski, F., Carey, S. J., & Menten, K. M. 2006b, A&A, 450, 569
Plambeck, R. L., & Menten, K. M. 1990, ApJ, 364, 555
Ragan, S. E., Bergin, E. A., & Wilner, D. 2011, ApJ, 736, 163
Rathborne, J. M., Jackson, J. M., & Simon, R. 2006, ApJ, 641, 389
Rathborne, J. M., Simon, R., & Jackson, J. M. 2007, ApJ, 662, 1082
Reach, W. T., Rho, J., Tappe, A., et al. 2006, AJ, 131, 1479
Reid, M. J., Menten, K. M., Zheng, X. W., et al. 2009, ApJ, 700, 137
Rosolowsky, E., Dunham, M. K., Ginsburg, A., et al. 2010, ApJS, 188, 123
Rosolowsky, E., & Leroy, A. 2006, PASP, 118, 590
Rosolowsky, E. W., Pineda, J. E., Foster, J. B., et al. 2008, ApJS, 175, 509
Sato, M., Hirota, T., Reid, M. J., et al. 2010, PASJ, 62, 287
Shepherd, D. S., Povich, M. S., Whitney, B. A., et al. 2007, ApJ, 669, 464
Smith, H. A., Hora, J. L., Marengo, M., & Pipher, J. L. 2006, ApJ, 645, 1264
Smith, M. D., & Rosen, A. 2005, MNRAS, 357, 1370
Sridharan, T. K., Beuther, H., Schilke, P., Menten, K. M., & Wyrowski, F. 2002, ApJ, 566, 931
Stahler, S. W., & Palla, F. 2005, The Formation of Stars (New York: Wiley-VCH)
Szymczak, M., Pillai, T., & Menten, K. M. 2005, A&A, 434, 613
Takano, S., Nakai, N., & Kawaguchi, K. 2002, PASJ, 54, 195
Urquhart, J. S., Hoare, M. G., Lumsden, S. L., et al. 2009, A&A, 507, 795
Urquhart, J. S., Hoare, M. G., Lumsden, S. L., Oudmaijer, R. D., & Moore, T. J. T. 2008, in ASP Conf. Ser. 387, Massive Star Formation: Observations Confront Theory, ed. H. Beuther, H. Linz, & T. Henning (San Francisco, CA: ASP), 381
Urquhart, J. S., Morgan, L. K., Figura, C. C., et al. 2011, MNRAS, 418, 1689
Voronkov, M. A., Brooks, K. J., Sobolev, A. M., et al. 2006, MNRAS, 373, 411
Voronkov, M. A., Caswell, J. L., Ellingsen, S. P., & Sobolev, A. M. 2010, MNRAS, 405, 2471

Voronkov, M. A., Caswell, J. L., Ellingsen, S. P., et al. 2012, in IAU Symp., 287, Cosmic Masers—from OH to H_0, ed. R. S. Booth, E. M. L. Humphreys, & W. H. T. Vlemmings (Cambridge: Cambridge Univ. Press), 433
Walsh, A. J., Breen, S. L., Britton, T., et al. 2011, MNRAS, 416, 1764
Wang, Y., Zhang, Q., Rathborne, J. M., Jackson, J., & Wu, Y. 2006, ApJL, 651, L125
Wang, K., Zhang, Q., Wu, Y., & Zhang, H. 2011, ApJ, 735, 64
Xu, Y., Li, J. J., Hachisuka, K., et al. 2008, A&A, 485, 729
Ybarra, J. E., & Lada, E. A. 2009, ApJL, 695, L120
Ybarra, J. E., Lada, E. A., Balog, Z., Fleming, S. W., & Phelps, R. L. 2010, ApJ, 714, 469
Zhang, Q., & Ho, P. T. P. 1995, ApJL, 450, L63
Zhang, Q., Hunter, T. R., Sridharan, T. K., & Cesaroni, R. 1999, ApJL, 527, L117
Zhang, B., Zheng, X. W., Reid, M. J., et al. 2009, ApJ, 693, 419